

Advanced light trapping scheme in decoupled front and rear textured thin-film silicon solar cells

Isabella, O.; Vismara, R.; Linssen, D.N.P.; Wang, K.X.; Fan, S.; Zeman, M.

DOI

[10.1016/j.solener.2018.01.040](https://doi.org/10.1016/j.solener.2018.01.040)

Publication date

2018

Document Version

Final published version

Published in

Solar Energy

Citation (APA)

Isabella, O., Vismara, R., Linssen, D. N. P., Wang, K. X., Fan, S., & Zeman, M. (2018). Advanced light trapping scheme in decoupled front and rear textured thin-film silicon solar cells. *Solar Energy*, 162, 344-356. <https://doi.org/10.1016/j.solener.2018.01.040>

Important note

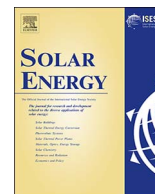
To cite this publication, please use the final published version (if applicable). Please check the document version above.

Copyright

Other than for strictly personal use, it is not permitted to download, forward or distribute the text or part of it, without the consent of the author(s) and/or copyright holder(s), unless the work is under an open content license such as Creative Commons.

Takedown policy

Please contact us and provide details if you believe this document breaches copyrights. We will remove access to the work immediately and investigate your claim.



Advanced light trapping scheme in decoupled front and rear textured thin-film silicon solar cells

O. Isabella^a, R. Vismara^{a,*}, D.N.P. Linssen^a, K.X. Wang^{b,c}, S. Fan^b, M. Zeman^a

^a Delft University of Technology, Photovoltaic Materials and Devices Laboratory, Mekelweg 4, 2628CD Delft, The Netherlands

^b Department of Electrical Engineering, Stanford University, Stanford, CA 94305, USA

^c School of Physics, Huazhong University of Science and Technology, Wuhan, China

ARTICLE INFO

Keywords:

Light management
Opto-electrical modelling
Thin-film solar cells
Wave guiding
Temporal mode-coupled theory
Absorption limit

ABSTRACT

We present the study of an advanced light trapping scheme applied to thin-film silicon-based solar cells, overcoming the broadband Green absorption limit, that is the generalized case of the $4n^2$ classical absorption limit for all wavelengths. This result is achieved by the 3-dimensional optical modelling of a fully functional thin-film hydrogenated nano-crystalline silicon (nc-Si:H) solar cell endowed with decoupled front and back textures. Our results stem from rigorously characterized optical properties of state-of-the-art materials, optimized geometric nano-features on the front and rear surfaces of the solar cell, and thickness optimization of the front transparent oxide. The simulated improvements derive from a gain in light absorption, especially in the near-infrared part of the spectrum close to the band gap of nc-Si:H. In this wavelength region, the material is weakly absorbing, whereas we now find significant absorption peaks that can only be explained by the concurrent excitation of guided resonances by front and rear textures. This insight indicates the need to modify the temporal coupled-mode theory, which fails to predict the absorption enhancement achieved in this work, extending its validity to the case of decoupled front/back texturing. Our approach results in substantially high photocurrent density ($> 36 \text{ mA/cm}^2$), creating a platform suitable for high efficiency single and multi-junction thin-film solar cells based either on typical silicon alloys or on the novel and promising barium (di)silicide (BaSi_2) absorber. In the latter case, using the same advanced light trapping employed for nc-Si:H, we demonstrate a very high implied photocurrent density of 41.1 mA/cm^2 , for a device endowed with $2\text{-}\mu\text{m}$ thick absorber.

1. Introduction

Solar cells based on silicon as light absorber currently dominate the photovoltaic (PV) market (Fraunhofer ISE, 2017; ITRPV Eighth Edition, 2017). Next to record solar cells fabricated on wafers of crystalline silicon (c-Si) (Battaglia et al., 2016; Glunz et al., 2015; Masuko et al., 2014; Yamamoto, 2015; Yoshikawa et al., 2017; Zhao et al., 1998), thin-film silicon multi-junction solar cells (TFSSC) based on alloys of hydrogenated amorphous silicon (a-Si:H) have been recently reported to have initial conversion efficiencies up to 16.3% (Kim et al., 2013; Liu et al., 2015; Söderström et al., 2012; Yan et al., 2011) and record stabilized conversion efficiency up to 14% (Sai et al., 2016). Even though this PV technology currently realizes lower conversion efficiency than other thin-film technologies, such as CIGS (Solar Frontier, 2015), CdTe (First Solar, 2016), perovskites (Yang et al., 2015), and GaAs (Alta Devices, 2013), it displays the smallest cell-to-module losses (Haug and Ballif, 2015), with demonstrated industrial-scale flexible (Guha and Yang, 2005; Jäger et al., 2013) and rigid modules (Gabriel et al., 2011;

TEL SOLAR, 2014; Vetter et al., 2009; Yamamoto et al., 2005) up to 6.5-m^2 wide area. That is, this technology is industrially mature in terms of nanometric-scale thickness uniformity, hundreds of Megawatt-scale throughput, and resilience against moisture (Haug and Ballif, 2015). For these reasons, thin films developed for a-Si:H-based solar cells constitute instrumental building blocks in current record c-Si solar cells (Masuko et al., 2014; Yamamoto, 2015; Yoshikawa et al., 2017) achieved industrially at wafer (i.e. large area) level. In addition, due to the lower absorption coefficient of a-Si:H alloys with respect to other PV absorber materials (Isabella, 2013; Vismara et al., 2016), TFSSC technology is the best platform for testing at both lab- and industrial-scale a variety of photonic approaches aimed to enhance the absorption of light in thin dielectric slabs (random/periodic texturing, dielectric spacers and reflectors, metallic nano-particles, etc.) (Brongersma et al., 2014; Haug and Ballif, 2015; Martins et al., 2012; Pahud et al., 2013; Tan et al., 2012; Zeman et al., 2013).

Today's and next-generation high efficiency TFSSCs are and will be entirely dependent on two factors. The first is the fabrication of a-Si:H

* Corresponding author.

E-mail addresses: o.isabella@tudelft.nl (O. Isabella), r.vismara@tudelft.nl (R. Vismara), shanhui@stanford.edu (S. Fan).

alloys with band gap between 0.75 eV and 2 eV, to ensure high open-circuit voltage as well as wide utilization of the solar spectrum in multi-junction architectures (Isabella et al., 2014b). The second is the enforcement of an efficient *light trapping* scheme to maximize light absorption and thus to generate substantial short-circuit current density. The expression *light trapping* means the concurrent application of several light management techniques for (i) broadband light in-coupling at the front side of the (multi-junction) solar cell, (ii) light scattering inside the absorber layer(s) and (iii) high internal rear reflectance (Holman et al., 2013; Ingenito et al., 2014). Next to the optical properties of silicon-based absorbers and their bandgap, also their material properties needs to be considered. For amorphous absorbers with bandgap higher than 1.2–1.4 eV, the property to enhance is the resilience against light induced degradation (Kakinuma et al., 1983; Matsui et al., 2013; Staebler and Wronski, 1980), using triode-based plasma-enhanced chemical vapour deposition (Matsui et al., 2015) and/or varying deposition temperature and plasma compositions (Melskens et al., 2014; Stuckelberger et al., 2013). For nano-crystalline absorbers with bandgap lower than 1.2 eV (e.g. hydrogenated nano-crystalline silicon, nc-Si:H), properly designed light management is instead helpful for ensuring high photocurrent density while keeping the thickness in the range of 2–3 μm . This is to cope with the reduced electrical performance of the material with respect to higher quality c-Si when textured substrates are deployed (Sai et al., 2013b).

The maximization of the photocurrent density delivered by a fully functional single junction nc-Si:H solar cell is the primary aim of this study. The perspective is that a solar cell based on a low band gap nano-crystalline absorber material endowed with a light trapping scheme delivers a certain photocurrent density. This value can be interpreted as the sum of the photocurrent densities of a monolithically integrated multi-junction device. In this respect, the cell based on the nano-crystalline material is the bottom cell and the thicknesses of the (amorphous) top cells need only to be tuned to meet the current-matching condition (Isabella et al., 2014a). It follows that the maximization of light absorption in the bottom cell *alone* results in the maximized total photocurrent density available for a multi-junction device in which such bottom cell is deployed.

For enhancing the absorption of light, a commonly applied light management technique is the texturing of (internal) surfaces of the device to scatter incident light away from the specular direction. Random surface textures are customarily used in solar cells for this purpose (Berginski et al., 2008; Boccard et al., 2012; Hongsingthong et al., 2010; Isabella et al., 2011; Kambe et al., 2008; Sato et al., 1992; Tan et al., 2015; Tan et al., 2013). Periodic surface gratings are newer, but proven textures used in single and multi-junction devices and in both *superstrate* and *substrate* configurations (Biswas and Xu, 2011; Ferry et al., 2009; Isabella et al., 2008; Isabella et al., 2010; Paetzold et al., 2011; Sai et al., 2016; Sai et al., 2013b; Söderström et al., 2009; van Erven et al., 2010). Depending on the geometry of the grating and involved materials, such textures diffract light into discrete angles and can couple light into guided modes in the active layer (Söderström et al., 2010). Combined with a thin absorber and an efficient back reflector, periodic textures constitute an advanced light trapping scheme that can potentially induce an absorption enhancement beyond the classical *Tiedje-Yablonoitch* (TY) absorption enhancement limit (Tiedje et al., 1984) (see Section 3.4) by exciting absorption resonances (Yu et al., 2010a, b). In fact, recent findings on the limit of light absorption in the diffraction regime have shown that periodic surface textures are not only very useful from theoretical standpoint (Naqavi et al., 2013), but also enable the determination of design rules for the optimization of light in-coupling (Battaglia et al., 2012).

In a previous contribution (Wang et al., 2012), decoupled front and rear surface textures were considered to structure an ultra-thin c-Si absorber. Using the Rigorous Coupled Wave Analysis, the front and back surfaces were separately optimized for light trapping and anti-reflection, respectively, leading to broadband light absorption close to

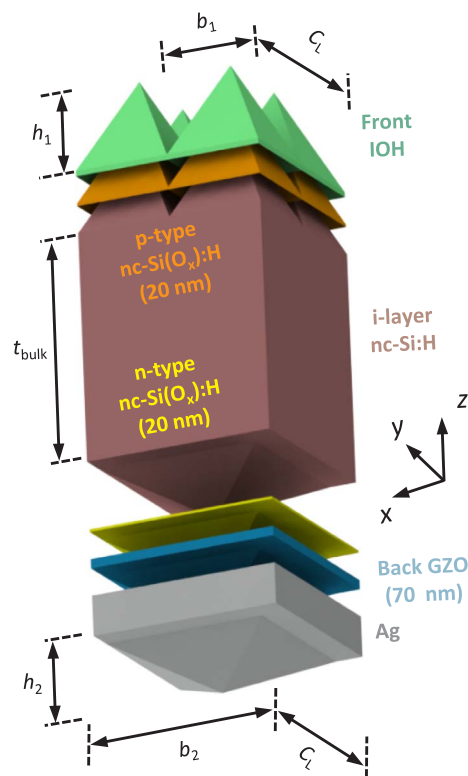


Fig. 1. 3-D view of a typical simulated unit cell with parameters defining the geometry of the front and the rear nano-pyramidal surface textures: front period (b_1) and height (h_1), rear period (b_2) and height (h_2), and common lattice (C_x) (see Section 3.2). Deployed layers in the solar cells are (from top to bottom): hydrogen-doped tin-oxide (IOH) as front TCO, p-type nc-Si(O_x):H, i-layer nc-Si:H, n-type nc-Si(O_x):H, gallium-doped zinc-oxide (GZO) as back TCO and silver. The shown unit cell is asymmetric with respect to its centre, due to non-commensurate front and rear nano-pyramids (see Section 2.1).

the classical TY absorption limit. In this study, starting from the concept of decoupled texturing, we shift the focus from structured and uncoated ultra-thin c-Si absorber slabs to fully functional thin-film solar cells based on structured nc-Si:H (see Fig. 1), appropriate as bottom cell in thin-film multi-junction devices (Zeman et al., 2013). The resulting performance is compared to the broadband *Green* absorption limit (Green, 2002) (see Section 3.4), which is the general case of the classical TY absorption enhancement limit.

At the front side of the device, high aspect ratio nano-pyramids arranged in a two-dimensional (2-D) rectangular lattice were used. This front texture of nano-pyramids enables efficient light in-coupling, as the spatially averaged effective refractive index nearly adiabatically varies from that of air to that of the silicon absorber (Ingenito et al., 2015; Isabella et al., 2016). At the rear side, nano-pyramids, also arranged in a 2-D rectangular lattice, were deployed, but this time with a lower aspect ratio (Zeman et al., 2013). Using this sort of structure, long wavelength photons close to the nc-Si:H bandgap can be efficiently scattered in several discrete directions. At the same time, the smaller height reduces scattering of light into the metallic back reflector, which would lead to plasmonic losses in the metal. To model the structure of the complete solar cell, parasitic optical losses in the layers surrounding the absorber were considered using rigorously characterized optical properties of state-of-the-art materials. Deploying an optical modelling software based on three-dimensional (3-D) Finite Element Method (FEM) (ANSYS), we could accurately simulate absorbance and reflectance spectra (Isabella et al., 2013) as well as calculate the implied photocurrent density related to each layer of the device. Furthermore, the spectral position of peaks in the absorbance curve of the absorber layer was explained by means of waveguide mode theory.

The optimization of both front and rear textures consisted of four

phases. In phase *zero* (see Section 3.1.1), non-commensurate front and rear periodicities were compared, to determine whether an asymmetric design could yield higher absorptance compared to its symmetric counterpart. In phase *one* (see Section 3.1.2), the height and the period of front and rear nano-pyramids were varied (see Fig. 1). The three best performing structures from phase *one* were considered in phase *two* (see Section 3.1.3). Here, the optical performance of the cell in presence of a so-called metal-oxide rear interface was evaluated. Specifically, between the intrinsic absorber material (i-layer) and the silver back contact, the use of an n-type hydrogenated nano-crystalline silicon oxide (nc-SiO_x:H) layer in place of the standard n-type nc-Si:H was tested, both with and without gallium-doped zinc oxide (ZnO:Ga, GZO) (Fujiwara and Kondo, 2005) in the role of back transparent conductive oxide (TCO). In this phase, the aim was to reduce both parasitic absorption and plasmonic losses in the textured metallic reflector (Demontis et al., 2013; Springer et al., 2004). In phase *three* (see Section 3.1.4), the thickness of the used front TCO, hydrogen-doped indium oxide (In₂O₃:H, IOH) (Koida et al., 2008), was optimized, to further decrease optical losses, particularly at short wavelengths. To finalize the study, the optical performance of the optimized structure for different angles of light incidence was evaluated (see Section 3.5).

Throughout each phase, the absorber layer thickness was kept constant to a volumetric equivalent value of 2 μm (see Section 2.3). In the best cases of perpendicular and tilted illumination on the optimized solar cell, we observed unprecedented implied photocurrent densities values of 36.00 mA/cm² and 36.84 mA/cm², respectively, corresponding to 0.31% and 2.64% enhancement compared to the *Green* limit calculated for the same optical equivalent thickness and assuming perpendicular incidence. These values of photocurrent densities, if successfully implemented in state-of-the-art triple junction or in next generation quadruple junction solar cells (Kirner et al., 2015; Liu et al., 2017; Schüttauf et al., 2015; Si et al., 2017, Si et al., 2014), may enable conversion efficiencies close to 20% in < 5-μm thick devices.

Finally, the outlook of this work follows two routes (see Section 4). In the first, we indicate how far our record light trapping scheme applied in single junction nc-Si:H solar cell is with respect to the best experimental counterparts and what can be still done at experimental level to come closer to our ideal optical behaviour. In the second, we show the optical potential of barium (di)silicide (BaSi₂) (Vismara et al., 2016), a novel absorber material with band gap close to that of c-Si (1.25 eV) (Suemasu, 2015). By deploying the same solar design optimized for nc-Si:H but endowed with BaSi₂, we demonstrate an implied photocurrent density of 41.1. mA/cm². This is particularly appealing, considering that similar values are achieved in front/rear contacted heterojunction c-Si solar cell (Yamamoto, 2015), which utilizes similar supporting layers but is two orders of magnitude thicker.

2. Methods and theoretical framework

2.1. 3-D optical modelling

The software used for the optical modelling is based on the rigorous solution of Maxwell equations via 3-D FEM (ANSYS). This method was chosen over others for three main reasons. First, the mesh calculated by FEM algorithms that describes the volume of each (thin) layer follows the actual geometry of the interfaces between different materials (i.e. no stair-case approximation) (Ritz, 1909; Weiland, 1977; Yee, 1966). Second, FEM-based algorithms feature very fast calculations in a 3-D space if an adequate amount of random access memory is available (Davidson, 2010). Third, the wavelength-dependent optical properties of the materials involved in the simulations can be used as-measured (i.e. no fitting of refractive index n and extinction coefficient κ is required) (Isabella et al., 2013). In this respect, Fig. 2 shows the optical properties of all the materials deployed in this study.

The effect of surface textures on light absorption in each modelled device was evaluated by calculating the so-called implied photocurrent

density (J_{ph}) associated to the absorptance in each layer or to the device reflectance (Isabella et al., 2014a; Isabella et al., 2013). The J_{ph} related to supporting layers (TCOs, doped layers, silver) or reflectance provides a measure of the optical losses in the simulated device. On the other hand, the implied photocurrent density of the absorber i-layer (J_{ph-i}) is the maximum photocurrent density achievable by a real device, as the electrical losses are in this case neglected. For this reason, J_{ph-i} was used as parameter for selecting the best structures to optimize from phase to phase and for calculating the figure of merit known as Light Trapping Efficiency (LTE) (Schuster et al., 2014) (see Section 2.5). It is worth noting that, due to the use of a silver back reflector, the J_{ph} related to transmittance was found to be numerically negligible at all wavelengths.

2.2. Solar cells structure

A schematic view of the typical solar cell deployed in our simulations was presented in Fig. 1. This figure shows what we define a *unit cell*: the smallest indivisible piece of a solar cell that is still recognizable as such. The squared common lattice, C_L^2 , is the xy-area of the unit cell; that is the area within which both front and rear nano-pyramids can be accommodated. When repeated in a 2-D pattern, the unit cell forms a full solar device at macroscopic scale and the nano-pyramids form the surface textures.

The geometry of the nano-pyramids is given by their height h_m and base width or period b_m , where $m = 1$ is used for the front surface and $m = 2$ for the rear surface. The thickness of the intrinsic nc-Si:H that does not include the nano-pyramids is called bulk thickness (t_{bulk}). A 3-D model was prepared for every structure in our parameter space. On the front surface, high aspect ratio nano-pyramids were explored, as the height was varied between 500 and 900 nm, while the base width was varied between 300 nm and 700 nm (Wang et al., 2012). On the rear surface, shallower nano-pyramids were deployed, as the height was varied between 100 nm and 500 nm and the base width was varied between 800 nm and 1200 nm (Isabella et al., 2012; Lipovšek et al., 2010). As it will be discussed in the next section, each combination of dimensions of front and rear nano-pyramids determined t_{bulk} .

Certain combinations in the chosen parameter space resulted in non-commensurate base widths between front and rear side of the unit cell. To ensure reasonable simulation times (i.e. to limit the size of the simulated unit cell), we made use of the common lattice C_L along with the duty cycle. The latter is defined as $D_m = N_m \cdot b_m / C_L$, where N_m is the number of nano-pyramids, either at the front and or at the rear side of the model, along the x- or y-direction in the unit cell. The quantity $1 - D_m$ is a measure of the space left un-textured around the nano-pyramids either at the front or at the rear side. In the 3-D model shown in Fig. 1, $C_L = 2 \cdot b_1 > b_2$, resulting in perfectly packed front texture ($D_1 = 1$) and in an un-textured area around the rear nano-pyramid ($D_2 = b_2 / C_L < 1$). In other 3-D models evaluated in this study, the case $C_L = b_2 > 2 \cdot b_1$ was also handled, that on the contrary left an un-textured area around the front nano-pyramids. In Section 3.1.1, we will discuss the effect of placing the nano-pyramids at the front or at the rear side (a) symmetrically with respect to the centre of the C_L^2 area.

To conclude this section, at the front side of the unit cell, we considered 20-nm thick p-layer and 100-nm thick front IOH TCO (in phase *three* the latter is thinned down to 40 nm, see Section 3.1.4). At the rear side of the unit cell, we considered 20-nm thick n-layer, 70-nm thick back GZO TCO and 300-nm thick silver reflector. For all these thin supporting layers, a geometry conformal to the nc-Si:H i-layer endowed with front and rear nano-pyramids was assumed.

2.3. Volumetric and optical equivalent thickness

The reference thickness (t_{ref}) of high efficiency single junction nc-Si:H solar cells is 2000 nm (Sai et al., 2013a, 2013b). As the number of photons absorbed in the i-layer is directly proportional to its volume

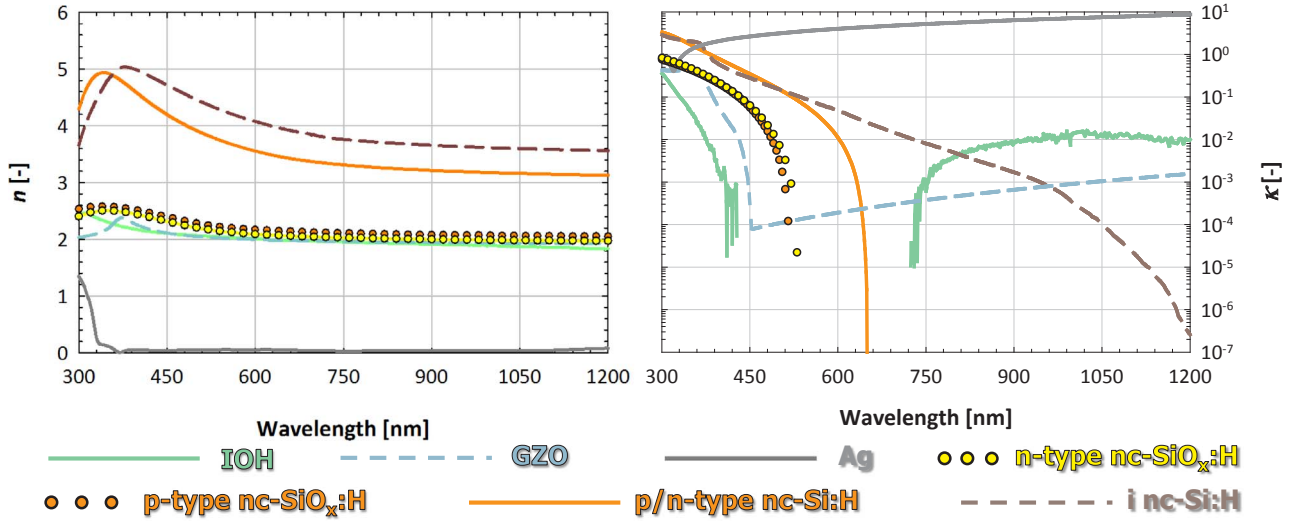


Fig. 2. Complex refractive index of each material used in this study: IOH (Koida et al., 2008), p-i-n nc-Si:H (Isabella et al., 2014a), p-n nc-SiO_x:H (Tan et al., 2015), GZO (Fujiwara and Kondo, 2005) and Ag (Isabella et al., 2014a). The real part is the refractive index n (left hand side panel); the imaginary part is the extinction coefficient κ (right hand side panel).

(Wang et al., 2012), the amount of absorber material in any simulated unit cell must stay the same for fair comparison. To fulfil such requirement in each simulated unit cell, an equivalent volume $V_{eq} = t_{veq} \cdot C_L^2$ was defined, where the volumetric equivalent thickness (t_{veq}) was kept constant at 2000 nm. Obviously, to account for the volume of the absorber material inside the front and rear nano-pyramids, t_{bulk} was varied to keep the volume V constant and equal to V_{eq} :

$$V = t_{bulk} \cdot C_L^2 + N_1^2 \cdot \frac{b_1^2 h_1}{3} + N_2^2 \cdot \frac{b_2^2 h_2}{3}, \quad (1)$$

t_{bulk} can be determined by equating V and V_{eq} :

$$t_{bulk} = t_{veq} - \frac{1}{3} (D_1^2 \cdot h_1 + D_2^2 \cdot h_2) \quad (2)$$

Next to the proportionality between absorbed photons and absorber volume, it should be noted that a front and rear textured i-layer is optically active from the uppermost to the bottommost morphological features (Schuster et al., 2014). This means that not only the t_{bulk} but also the peak-to-valley height of the front and of the rear features must be considered. In this respect, optical thickness was defined as follows:

$$t_{opt} = h_1 + t_{bulk} + h_2 \quad (3)$$

In summary, for each simulated unit cell, Eq. (2) was used to set up the bulk thickness of i-layer and Eq. (3) to assess its optical performance with respect to the light absorption limits (see next section).

2.4. Light absorption limits and flat equivalent cell

In this section, we briefly review the analytical models that describe the lowest and highest absorption of light in a dielectric slab. These were used to evaluate the quality of the proposed light trapping scheme applied to realistic solar cell structures. The first fundamental concept to introduce is the *single-pass* light absorption. In a flat slab, assuming broadband perfect front light in-coupling (i.e. no front reflectance), no back reflector and perpendicular incidence of light, photons can pass through only once. The amount of absorbed light is thus described by Lambert-Beer's law:

$$A_{SP} = 1 - e^{-\alpha d} \quad (4)$$

where $\alpha = 4\pi\kappa/\lambda$ is the wavelength-dependent absorption coefficient of the dielectric material and d is the thickness of the slab. Single-pass absorption is used in this contribution as reference (i.e. lower limit) to calculate the absorption enhancement factor (EF), which is defined as the ratio between calculated (or simulated) absorption in the i -th layer

(A_i) and A_{SP} ($EF_i = A_i/A_{SP}$).

When a lossless ideal back reflector is implemented in such an optical system, any light that could pass through the slab unabsorbed will now experience a second pass, partly being absorbed and partly leaving the slab at the front side (the so-called *double-pass* light absorption, DP). In this situation, the optical thickness of the slab doubles, and the amount of absorbed light can be described as follows:

$$A_{DP} = 1 - e^{-2\alpha d} \quad (5)$$

As expected, in the weak absorbing region of the dielectric slab (i.e. $\alpha d \ll 1$), $EF_{DP} = A_{DP}/A_{SP} = 2$. That is, in this part of the spectrum, absorption is doubled with respect to the single-pass case, owing to the presence of a lossless back reflector.

The classical TY limit is the most widely used model for benchmarking the performance of simulated or real dielectric slabs and solar cells. In addition to the assumptions of the double pass limit (i.e. perfect light in-coupling at the front side and ideal reflection at the back), ideal isotropic light scattering is enforced inside the slab. This makes the optical thickness of the dielectric slab much greater than twice the real thickness. The formulation of such light absorption limit is the following:

$$A_{TY} = \frac{4n^2\alpha d}{1 + 4n^2\alpha d} \quad (6)$$

where n is the real part of the material refractive index. Although Eq. (6) can be computed for every wavelength, it holds its physical meaning only in the weak absorbing region of the spectrum (i.e. $\alpha d \ll 1$). In these conditions, the enhancement factor of the TY limit tends to the well-known $4n^2$ value.

A generalization of the TY light absorption limit that can be applied to the whole wavelength range was proposed by Green (Green, 2002):

$$A_{Green} = \frac{1 - e^{-4\alpha d}}{1 - \left[1 - \frac{1}{n^2}\right] e^{-4\alpha d}} \quad (7)$$

Note that in the weak absorbing region, if $n^2 > 1$, a linear approximation can be applied to reduce Eq. (7) to Eq. (6), obtaining the expression of the TY limit once again. Comparing Eq.7 and Eq. (6), the so-called *Green* absorption limit will have slightly higher values than the TY limit, making it harder to surpass.

For every textured solar cell, it is possible to consider its flat equivalent (FE) structure. In contrast to the un-coated dielectric slab used to calculate the single pass limit or the *Green* limit, the flat equivalent cell is a fully functional device. That is, each layer

considered in this FE solar cell is the same (material and thickness) as in its textured counterpart. The only difference is the thickness of the i-layer, which in the FE architecture is set to t_{opt} . The absorption of the FE cell is not a limit *per se*, but it is similar to the DP limit, due to its flat interfaces and to the presence of a back reflector. However, the absorption in an FE cell is less than the DP limit, because of the non-ideal front in-coupling and back reflector, and due to parasitic absorption in supporting layers.

Similarly to the J_{ph} associated to simulated spectra, the implied photocurrent density associated to light absorption limits (J_{DP} and J_{Green}) or to the i-layer absorptance of the FE cell (J_{FE}) can be computed. In particular, J_{Green} is considered the benchmark value, and the significance of the computed $J_{\text{ph-i}}$ of every modelled structure is quantified by calculating its deviation from J_{Green} :

$$\Delta_{\text{Green}} = \frac{(J_{\text{ph-i}} - J_{\text{Green}})}{J_{\text{Green}}} \% \quad (8)$$

2.5. Light trapping efficiency

Light Trapping Efficiency (*LTE*) is a figure of merit for the comparison of the optical performance of solar cells (Schuster et al., 2014). As previously mentioned, authors commonly use the classical $4n^2$ limit to assess the performance of light trapping schemes. However, this is of limited use when comparing results across studies, because the deviation from such limit strongly depends on the absorber thickness and on the materials chosen for the eventual supporting layers. *LTE* as a comparison tool circumvents device specifics, and allows to compare results here presented to previously obtained results, whether numerical or experimental. Concretely, *LTE* is defined as:

$$LTE = \frac{J_{\text{ph-i}} - J_{\text{FE}}}{J_{\text{Green}} - J_{\text{DP}}} \quad (9)$$

For the numerator of *LTE* two rigorous simulations are needed, to carry out the implied photocurrent density of the i-layer in a textured solar cell and in the corresponding FE structure ($J_{\text{ph-i}}$ and J_{FE} , respectively). As for the denominator, J_{Green} and J_{DP} are calculated with Eq. (7) and Eq. (5), respectively. Notice that $LTE = 1$ is extremely difficult to achieve or overcome, because the reference structures (FE, *Green* and DP slabs) are computed for t_{opt} , which is always equal or larger than t_{bulk} . This results in a numerator generally smaller than the denominator, unless an advanced light trapping scheme is enforced in the textured cell.

2.6. Wave guiding and reflection pole method

The light trapping scheme here discussed is based on the decoupled texturing of the front and rear side of the nc-Si:H slab. This texturing approach enhances light absorption in the i-layer, ensuring a high $J_{\text{ph-i}}$ by triggering (i) broadband light in-coupling, (ii) efficient light scattering and (iii) high rear internal reflectance, owing to the presence of the back reflector.

The decoupled texture effectively couples plane waves impinging on the solar cell into wave-guided modes allowed within its thin films (including the i-layer). In other words, light passes from vertical incidence on the textured front surface to horizontal propagation and (partial) absorption in the thin layers beneath. In a real solar cell with flat interfaces, due to energy and momentum conservation (Haug et al., 2011a, 2011b), wave-guided modes may not be excited by perpendicularly incident radiation. However, in structured solar cells such excitation may occur, mediated by randomly or periodically textured interfaces (Haug et al., 2011a, 2011b). As long as the surface roughness stays in the range of geometric dimensions for which diffraction applies, resonances in the A_i spectrum (Yu et al., 2010b) indicating wave-guiding excitation can be associated to the wave-guided modes

available in the FE cell (Haug et al., 2009; Söderström et al., 2010).

In the diffraction regime, the main difference between random and periodic textures is the wavelength-dependent distribution and intensity of resonances related to wave-guided modes in the A_i spectrum (Battaglia et al., 2012). Since random textures are the superposition of an infinite number of sinusoidal gratings, they scatter light continuously over all angles, albeit with weaker intensity for larger scattering angles and longer wavelengths (Jäger et al., 2011). That is, random textures can couple light to all wave-guided modes available in the i-layer within a continuum of wavelengths (i.e. energies). The resulting A_i spectrum is therefore much larger than the DP limit and smooth, as it is populated by a continuum of resonances with steadily decaying intensity towards long wavelengths. Supported by TCM theory (Suh et al., 2004), this sort of spectrum can come very close to the classical $4n^2$ TY limit or in general to the *Green* limit but cannot overcome them (Yu et al., 2010b). On the other hand, since periodic textures scatter light only at well-defined angles (Jäger et al., 2011), they can strongly couple light to wave-guided modes available in the i-layer only at specific wavelengths (Yu et al., 2010b). In this case, the resulting A_i spectrum is populated by distinct resonances, whose intensity can be higher than both TY and *Green* limits although only in narrow wavelength bands. For an absorber endowed with 2-D gratings based on a square (triangular) lattice with periodicity P , such resonances can overcome the *Green* limit and achieve an $EF/4n^2$ up to π ($2\pi/\sqrt{3}$) when $\lambda/P = 1$ ($\lambda/P = \sqrt{3}/2$) (Yu et al., 2010a, b). Such an enhancement, however, (i) does come together with an enhanced angular sensitivity of the cell (Yu and Fan, 2011; Yu et al., 2010a) and (ii) does not represent the absolute limit achievable with any light trapping scheme. In fact, for diffraction gratings and for $\lambda/P \rightarrow 0$, the upper limit approaches the thermodynamic limit (Mellor et al., 2011) ($EF = 4n^2/\sin^2(\theta_0)$, where θ_0 is the half angle of the illumination cone). Nevertheless, the regime $\lambda \approx P$ is where it is easier to come close to such an upper limit with relatively simple grating designs (Mellor et al., 2011).

In the simulated solar cells of this contribution, as shown in Section 3.3, resonances in the A_i spectrum related to excited wave-guided modes could be mediated by the top grating, by the bottom grating or by both gratings. To reveal the nature of such resonances in decoupled textured solar cells, and to monitor their spectral position, the Reflection Pole Method (Anemogiannis et al., 1999; Shakir and Turner, 1982) (RPM) was employed. This numerical method, which has been successfully applied on multilayer structures resembling functional solar cells (Naqavi et al., 2014), correlates the poles of the reflection coefficient of a flat multilayer stack with therein supported wave-guided modes of the parallel component of the electro-magnetic field propagation vector (k_{\parallel}) (Haug et al., 2012; Söderström, 2013). Note that the RPM evaluates flat multilayer structures but it has been experimentally proven meaningful also for textured thin-film solar cells (Haug et al., 2011a, 2011b).

Referring to the FE cell of the textured device sketched in Fig. 1, five dielectric layers (1 = front TCO, 2 = p-layer, 3 = i-layer, 4 = n-layer, 5 = back TCO) are sandwiched between air at the front side and the silver cladding at the rear side. The RPM can be then briefly described as follows: Error! Reference source not found. First, the propagation constant S_j in the j^{th} dielectric layer must be determined:

$$S_j = \sqrt{k_j^2 - k_{\parallel}^2} = ik_j \sqrt{\frac{k_j^2}{k_{\parallel}^2} - \varepsilon_j} \quad (10)$$

where ε_j and k_j are the wavelength-dependent complex dielectric constant and the modulus of the wave vector in the j^{th} layer, respectively, and i indicates the imaginary unit. The values of S_j are normally determined by sweeping the relevant range of k_{\parallel} values. Second, the reflection coefficients at each interface in the multilayer stack can be computed, for both P and S polarizations ($r_{j,j+1}^{\text{P}}$ and $r_{j,j+1}^{\text{S}}$). For $j = 1$, the reflection coefficients at the interface between the first and the second layer can be determined:

$$r_{12}^p = \frac{\epsilon_1 S_2 - \epsilon_2 S_1}{\epsilon_1 S_2 + \epsilon_2 S_1} \tag{11}$$

$$r_{12}^s = \frac{S_1 - S_2}{S_1 + S_2} \tag{12}$$

Finally, for the complete stack consisting of five dielectric layers, it is possible to calculate the reflection coefficient at the front side with the following recursive expression, which is the same for both polarizations:

$$r_{12345} = \frac{r_{12} + \frac{r_{23} + \frac{r_{34} + r_{45} \exp(2i \cdot S_4 d_4)}{1 + r_{34} r_{45} \exp(2i \cdot S_4 d_4)} \exp(2i \cdot S_3 d_3)}{1 + r_{23} \frac{r_{34} + r_{45} \exp(2i \cdot S_4 d_4)}{1 + r_{34} r_{45} \exp(2i \cdot S_4 d_4)} \exp(2i \cdot S_3 d_3)} \exp(2i \nu S_2 d_2)}{1 + r_{12} \frac{r_{23} + \frac{r_{34} + r_{45} \exp(2i \cdot S_4 d_4)}{1 + r_{34} r_{45} \exp(2i \cdot S_4 d_4)} \exp(2i \cdot S_3 d_3)}{1 + r_{23} \frac{r_{34} + r_{45} \exp(2i \cdot S_4 d_4)}{1 + r_{34} r_{45} \exp(2i \cdot S_4 d_4)} \exp(2i \cdot S_3 d_3)} \exp(2i \cdot S_2 d_2)} \tag{13}$$

where d_j is the thickness of the j^{th} layer and, in particular, $d_3 = t_{\text{opt}}$.

The RPM yields the reflection coefficient at the front of the FE cell as function of k_{\parallel} and λ . Its numerically relevant peaks are its poles and they follow specific patterns, corresponding to the wave-guided modes available in the five dielectric layers of the FE cell. Brillouin zones related to the periodicities of the front and back textures (and therefore to their diffraction modes) can be overlaid on this dispersion diagram. If one of the available wave-guided modes exists at the k_{\parallel} value corresponding to the centre of allowed Brillouin zones, then such wave-guided mode can be excited. Sampling the wavelength at which each resonance occurs in the A_i spectrum allows the matching to the excited wave-guided modes in the dispersion diagram (see Section 3.3).

3. Results and discussion

3.1. Structure optimization

3.1.1. Phase zero: non-commensurate geometries

Referring to the left panel of Fig. 3, the 3D-models presented in this study are in the first quadrant of the coordinate system ($x > 0$ and $y > 0$). For unit cells with either top or bottom duty cycle < 1 (see Section 2.2), the leftover space between pyramids allows to displace these textures away from each other. This causes a level of asymmetry that is dependent on the duty cycle (i.e. a smaller duty cycle allows for greater asymmetry). The right panel of Fig. 3 shows the spectral difference in absorbance of the i-layer (A_i) between a symmetric and an asymmetric structure obtained by diagonally displacing top and bottom textures. Results show that displacing such non-commensurate

geometries increases A_i across the whole wavelength range of interest.

It would be also possible to create a non-diagonal asymmetry by displacing the top and the bottom textures only in the x- or the y-direction. These cases are not reported here, since a diagonal displacement always creates the largest deviation with respect to the symmetric case. Further, asymmetric structures could be also created for commensurate geometries, for example by enforcing a duty cycle smaller than 1. Finally, pyramids could also be displaced and sliced in an arbitrary plane while still forming a perfect unit cell in an infinitely repeating pattern of pyramids. These approaches were not considered since our goal has always been to minimize the size of unit cells and their modelling complexity.

3.1.2. Phase one: sweeping geometrical parameters

A geometric optimization was first performed. The dimensions of the surface texture, described by the geometric attributes of the nano-pyramids, determine the diffraction of light and consequently its absorption. In our simulations, the morphologies of the pyramids on the top and bottom surfaces were separately varied in an ample parameter space, and optimized for maximum anti-reflection at the front and maximum near-infrared light diffraction at the back. By always assessing a combination of front and back textures, light absorption in the i-layer was maximized. The best performing structures from this first optimization phase have similar properties. Tall nano-scale pyramids at the front side of the device promote excellent in-coupling of light, by allowing for a smooth transition of the refractive index from air (incident medium) to the i-layer. At the rear side of the device, larger pyramids are necessary to diffract long-wavelength light, effectively extending its path length in the absorber. These features also need to be (relatively) shallow, to avoid significant parasitic absorption in the back reflector. The results of the three best performing structures can be reviewed in Table 1. The structure that achieves the highest absorption is asymmetric and it has top surface pyramids of $700 \times 700 \text{ nm}$ ($b \times h$) and bottom surface pyramids of $1200 \times 500 \text{ nm}$ with 200 nm of flat surface in both x- and y-direction to fill a common lattice (C_L) of 1400 nm (see Section 2.2). The simulated absorption was then integrated with the AM1.5 spectrum (NREL), to obtain an implied photocurrent density $J_{\text{ph-i}}$ (Isabella et al., 2014a) of 33.81 mA/cm^2 . After the material optimization described in phase two and three, however, it was found that structure #2 could achieve a higher optical performance than structure #1. Hence, from now on all results presented will concern structure #2 (asymmetric, $700 \times 700 \text{ nm}$ pyramids at the front, $1200 \times 300 \text{ nm}$ pyramids at the back side with 200 nm of flat surface in both x- and y-direction to fill $C_L = 1400 \text{ nm}$).

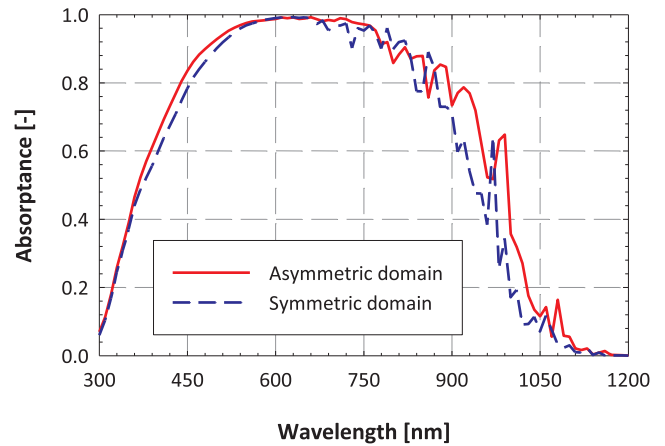
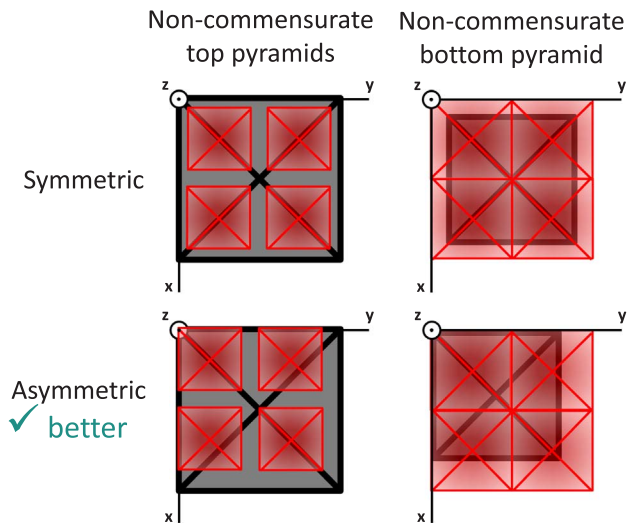


Fig. 3. Left panel: schematic top-to-down views of unit cells with non-commensurate top or bottom pyramids in symmetric and asymmetric simulation domains. Right panel: Example of absorption spectra A_i in simulated symmetric and asymmetric domains.

Table 1

Results of the three best structures, where b_m indicates the texture pyramid base, h_m the height and t_{bulk} the bulk thickness of the absorber layer; $m = 1, 2$ denotes the top and bottom surfaces, respectively. $J_{\text{ph-i}}$ is the predicted photocurrent from the cell, with ΔGreen the deviation from the photocurrent given by the Green limit (J_{Green}) computed with the same absorber optical thickness (t_{opt} , see Section 2.3). Note that the best performing structures have similar geometry. Since in all cases the bottom pyramids were non-commensurate ($D_2 < 1$, $C_L = 1400$ nm, see Section 2.2), an asymmetric design was employed.

Rank or structure	#1	#2	#3
b_1 [nm]	700	700	700
h_1 [nm]	700	700	900
b_2 [nm]	1200	1200	1200
h_2 [nm]	500	300	500
t_{bulk} [nm]	1644.2	1693.2	1577.5
$J_{\text{ph-i}}$ [mA/cm ²]	33.81	33.62	33.68
J_{Green} [mA/cm ²]	36.05	35.89	36.18

3.1.3. Phase two: metal-oxide rear interface

To further enhance the optical performance, it is useful to analyse and optimize the structure of supporting layers that – in combination with the absorber – form a complete solar cell device. These supporting layers are crucial for the optimal functioning of solar cells, but can also be an obstacle to achieve high optical performance. In particular, small amounts of light are absorbed in these layers, thus not contributing to the total photocurrent density generated in the solar cell. By reducing these parasitic losses, a significant gain in absorption in the i-layer can be obtained. To this purpose, four solar cell designs were investigated, each with a different combination of p-layer, n-layer and back TCO. Note that here we did not change the thickness of the supporting layers (front IOH: 100 nm, p-/n-layer: 20 nm, back GZO: 70 nm), but rather utilized different materials. The geometries of these devices are based on those of the three best performing structures from phase one (see Table 1). As mentioned above, the largest $J_{\text{ph-i}}$ value achieved in this phase was found for structure #2.

Materials and results are summarized in Table 2. Designs I and II employ p- and n-doped nc-Si:H, while designs III and IV use more transparent nc-SiO_x:H as doped layers. In addition, designs II and IV include a TCO layer between the n-doped layer and the back reflector, while design I and III do not. The function of this spacer layer is to improve the reflectivity at the back side, mainly by reducing parasitic absorption losses in the metallic contact (Demontis et al., 2013; Isabella et al., 2016; Santbergen et al., 2014). GZO was chosen as back TCO, owing to its high transparency and conductivity. In addition, its presence shifts plasmonic resonance from the near infrared part of spectrum to shorter wavelengths, effectively quenching plasmonic losses in the silver layer, since higher-energy photons are absorbed by silicon before they can reach the semiconductor–metal interface.

Regarding the results, we first discuss the spectra reported in Fig. 4 for design I. Without a back-TCO and using doped nc-Si:H significant losses in the silver back reflector can be observed, attributed to the plasmonic effect, resulting in the lowest performance of all designs with $\Delta\text{Green} = -11.28\%$.

In this regard, a significant improvement in the absorption spectrum

Table 2

Solar cells with identical geometric properties (structure #2), but varying performance depending on supporting layer materials.

Structure	#2			
	I	II	III	IV
Back TCO	–	GZO	–	GZO
Doped layers	nc-Si:H	nc-Si:H	nc-SiO _x :H	nc-SiO _x :H
J_{ph} [mA/cm ²]	31.84	33.62	34.37	35.18
ΔGreen [%]	–11.28%	–6.33%	–4.24%	–1.99%

of the i-layer is achieved by design II, where a back-TCO is included. Absorption losses related to the silver layer have been quenched as plasmonic resonances have been blue-shifted. The resulting performance was recovered to $\Delta\text{Green} = -6.33\%$. In design III, the inclusion of doped nc-SiO_x:H layers, instead of regular nc-Si:H, is assessed. Without a back-TCO, parasitic losses in the silver layer are still apparent. They are however considerably smaller than in the case of doped nc-Si:H layers (without a back-TCO), owing to the lower refractive index of nc-SiO_x:H (i.e. n-doped nc-SiO_x:H acts both as doped layer and spacer to quench absorption in the metallic back contact). In the short wavelength region, parasitic losses in the p-layer have decreased (with respect to stacks I and II), due to the much larger band gap of nc-SiO_x:H, resulting in $\Delta\text{Green} = -4.24\%$. Finally, in design IV both doped nc-SiO_x:H supporting layers and GZO as back-TCO are included. Reintroduction of the GZO-layer further suppresses parasitic absorption in the back reflector, due to the larger spacing between the i-layer and the metal. This result in an additional increase of the absorption ($\Delta\text{Green} = -1.99\%$).

3.1.4. Phase three: sweeping front TCO thickness

Studying the spectral response in Fig. 4, some parasitic absorption losses in the front TCO can still be observed (green areas). For this layer, IOH is employed, a highly-transparent and conductive TCO commonly used in state-of-the-art thin-film silicon solar cells (Boccard et al., 2012; Sai et al., 2016; Si et al., 2014; Tan et al., 2015). In previous phases, the thickness of this layer was fixed to 100 nm. In this phase, we analyse the impact of having a thinner front TCO. Reducing the thickness of the front-TCO to improve the optical properties of the cell has a major drawback. A thinner front TCO will increase the series resistance of the cell, effectively reducing its fill factor. In a perspective of deploying our findings in current-matched multi-junction devices, it is expected that the short-circuit current density of the overall device is smaller than the one of the single junction here modelled, relaxing the requirement on the front TCO thickness (Battaglia et al., 2011). Therefore, a thickness sweep from 100 nm to 40 nm was conducted. The device model with the thinnest IOH layer (40 nm) managed to achieve an implied photocurrent density in the absorber of 36.0 mA/cm² (see Fig. 5) This value surpasses the Green-limit photocurrent (35.89 mA/cm²), demonstrating the excellent light-trapping capabilities of the proposed front and rear decoupled texture.

At this point in our study, we compare our results to those obtained by (Wang et al., 2012), on whose findings this work was based. We recall that Wang et al. also conducted a separate optimization of the top and bottom surfaces of his device, but only considered a textured c-Si slab with a volumetric equivalent thickness $t_{\text{veq}} = 2000$ nm (see Section 2.3). This means that parasitic losses in the surrounding layers, as they would occur in a real solar cell, were not considered. In our study, instead, the layers included in a state-of-the-art fully-functional solar cell were taken into account, therefore including all possible losses that can occur within a real device.

Consequently, losses in the short wavelength range of the spectrum from 300 nm to 450 nm can be still observed, owing to the presence of the front TCO and of the p-layer. Nonetheless, the absorption enhancement in the near infrared region is so pronounced that a significant improvement over previous results was achieved. Due to a minimization of parasitic losses and to the occurrence of guided modes (see Section 3.3), the simulated absorption in our i-layer is enhanced beyond the Green limit ($\Delta\text{Green} = +0.31\%$) and realizes a +11.56% improvement with respect to the results of the previous study. This significant increase of absorption can be mainly ascribed to a better trapping of infrared photons inside the absorber, promoted by the asymmetry of the structure and by the presence of lower refractive index supporting layers on both sides of the absorber. In particular, the p- and n-type nc-SiO_x:H films act similar to cladding in optical fibres, confining light inside the central high-refractive index material. While these layers are a significant source of parasitic absorption losses,

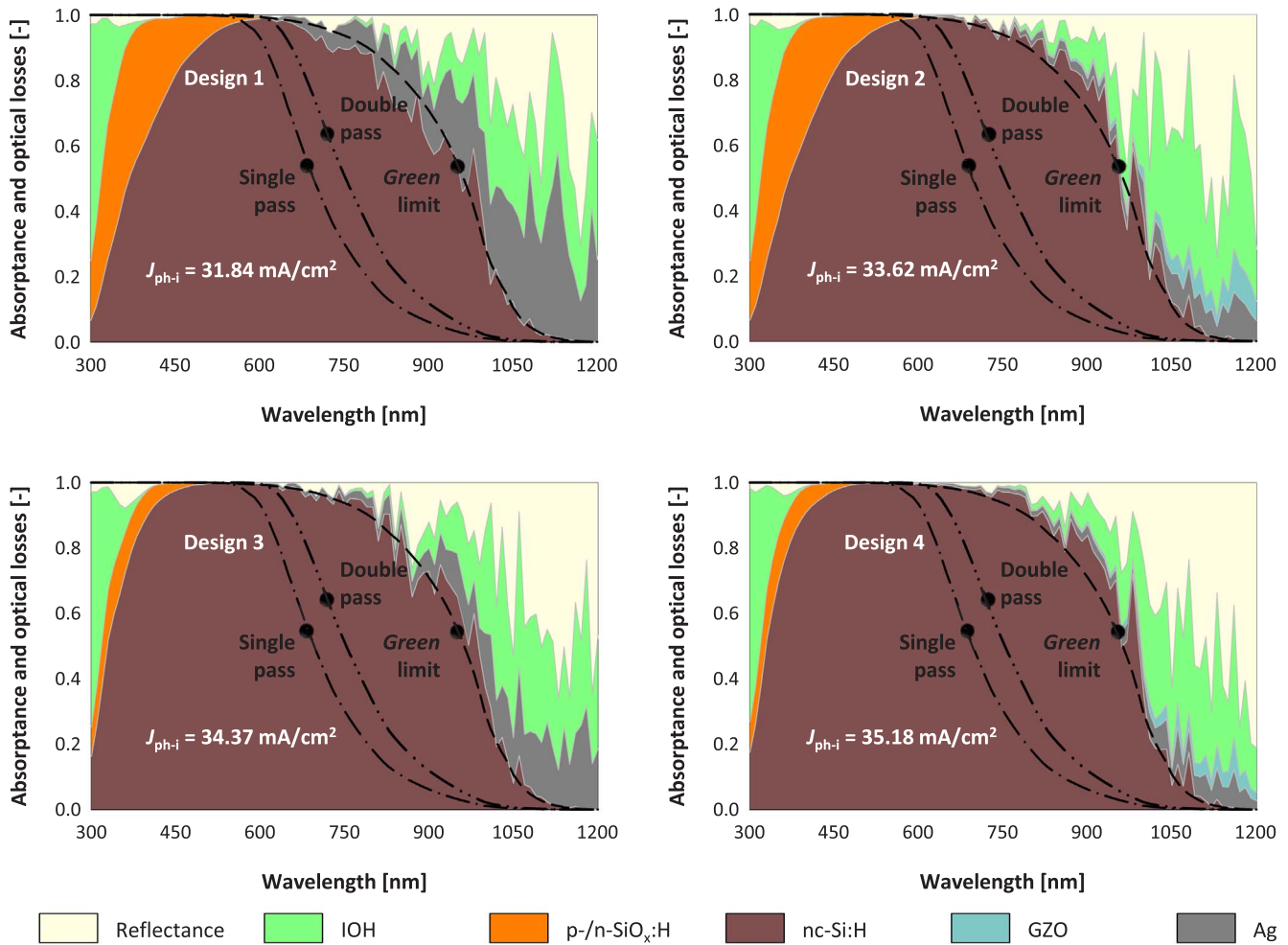


Fig. 4. Area plots for the four solar cell designs summarized in based on structure #2 (see). Single pass, double pass and Green limit implied photocurrent are 21.16 mA/cm², 24.72 mA/cm², and 35.89 mA/cm², respectively, for all configurations. Solar cells with doped nc-Si:H layer (1 and 2) exhibit large parasitic absorption, particularly at short wavelengths (orange area), while devices with no back GZO between n-doped layer and silver contact (1 and 3) display higher parasitic losses in the metal in the near infrared part of the spectrum (grey area).

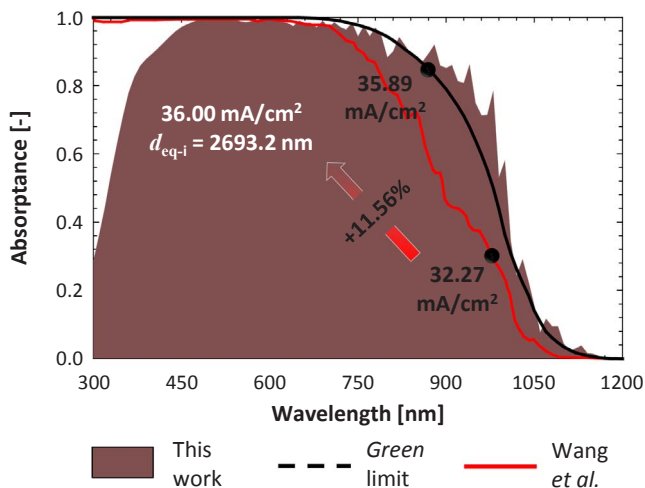


Fig. 5. Comparison of the results of this work (structure #2, design #4, 40-nm thick front IOH) and those obtained using the structure proposed by Wang et al. and the optical properties of presented in , resulting in an improvement of 11.56% and 0.31% with respect to previous work and the Green limit (35.89 mA/cm²), respectively.

particularly in the blue and UV regions, their presence appear to be quite beneficial – from an optical performance point of view – in the remaining part of the spectrum, where they are weak absorbers.

3.2. Electric field distribution and enhancement factor

To understand the reasons behind the excellent optical performance achieved by our optimized decoupled-textured model, it is worthwhile to look at the electric field distribution inside the structure. This distribution represents how light is propagating inside the device, thus providing an insight on which optical phenomena are taking place owing to the presence of the decoupled texture.

Let us consider a diagonal slice of the unit cell showing the electric field distribution at a wavelength of 650 nm (see Fig. 6, leftmost picture). Since silicon is highly absorptive at this wavelength, light is absorbed closer to the front of the device. There, resulting from light interacting with the front texture, it is possible to distinguish strong localized absorption enhancements inside the top pyramids. At the same time, we observe low intensity of the electric field at the rear side. At longer wavelengths, it is noticeable the electrical field propagating through the entire absorber thickness and interacting with the bottom part of the device. Several high-intensity regions with a periodic character can be observed at specific wavelengths (e.g. 980 nm, 1130 nm and 1190 nm in Fig. 6). Their presence suggests that the decoupled front/rear texture induces resonances in the nc-Si:H layer, thus enhancing the absorption. Also, it evidences that the absorber layer is acting as a waveguide (see Section 3.3), supporting in longitudinal direction approximately two periods at 980 nm, three periods at 1130 nm and possibly more at 1190 nm.

Currently, it is challenging to determine whether the electric field

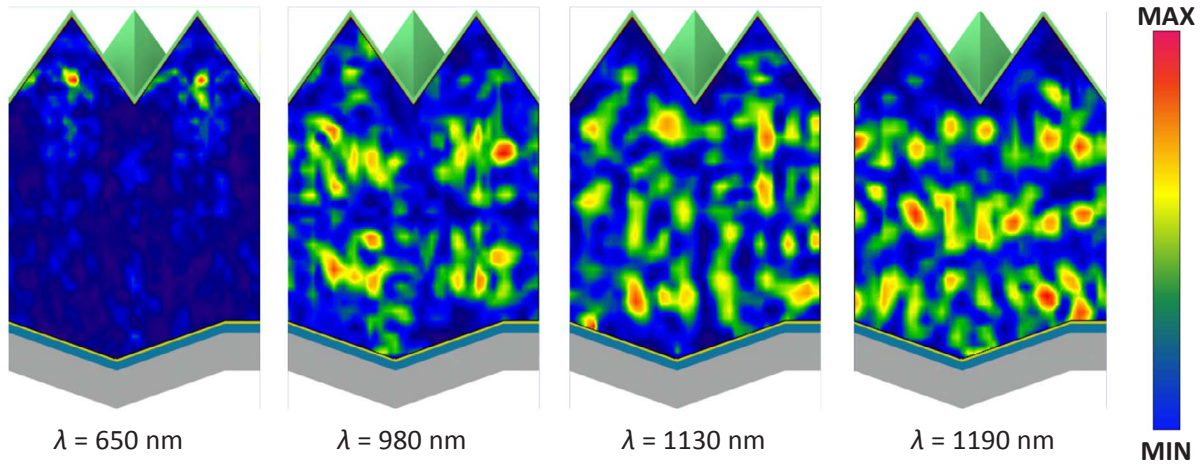


Fig. 6. Diagonal cross-section of the unit cell, depicting the electric field distribution in the absorber at several wavelengths of interest: 650 nm (leftmost), 980 nm (centre-left), 1130 nm (centre-right), and 1190 nm (rightmost).

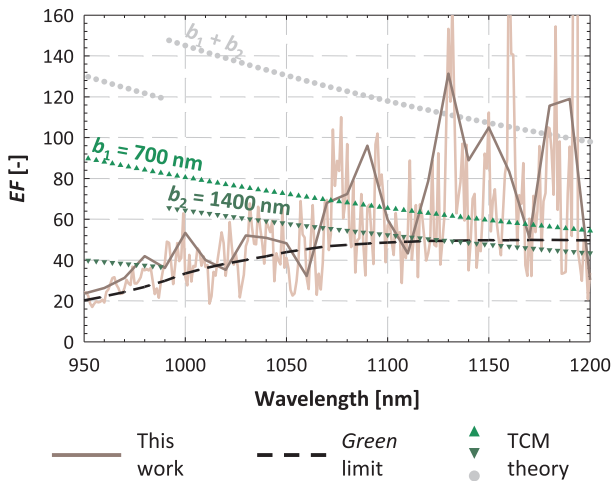


Fig. 7. Enhancement factor (EF) of the best model (structure #2, design #4, 40-nm thick front IOH), simulated each 10 nm (dark brown) and each 1 nm (light brown), compared to the maximum absorption enhancement calculated with the *Green* limit (black), and with the temporal coupled-mode (TCM) theory, using both the front (light green, up-triangles) and the back periodicity (dark green, down-triangles). Grey circles represent the sum of the EF values calculated separately for front and back periods.

distribution inside the absorber layer is more influenced by the front or by the back texture. However, it is nonetheless possible to show that both textures actively contribute to the absorption enhancement. In this respect, referring to Section 2.4, it is useful to compare the wavelength-dependent enhancement factor EF_i of the best modelled structure not only with the EF_{Green} ($EF_{Green} = A_{Green}/A_{Sp}$) but also with the theoretical maximum values calculated with the temporal coupled-mode (TCM) theory (Yu et al., 2010b) (see Fig. 6). For this purpose, to get higher spectral resolution in the wavelength range of interest, next to the 10-nm stepped absorption spectra so far reported, we also simulated the optical situation in our record structure at every one nm. The TCM theory predicts EF values beyond the conventional $4n^2$ limit for 2-D periodically-textured dielectric slabs with feature sizes in the same order of magnitude as the wavelength of incident light *in vacuo* (Yu et al., 2010a, b). The formula, derived by Yu et al. for a 2-D periodic square lattice (Yu et al., 2010a, b), was used to calculate the theoretical $EF(\lambda)$ depicted in Fig. 7. It is worth noting that such closed formula is valid in the over-coupling regime, that is when the rate of light absorption in the dielectric is significantly lower than the rate at which light is out-coupled (i.e. can escape from the absorber). In the Fig. 7, the upward-pointing triangles indicate the EF calculated using the period of

the front grating ($b_1 = 700$ nm), while the downward-pointing triangles were computed using the period of the back grating ($b_2 = 1400$ nm). For comparison only, the circles represent the sum of the two previously calculated EF curves.

As seen in Fig. 5 and as expected from the TCM theory, our modelled absorption spectra result in EF beyond that of *Green* limit at specific wavelengths. The simulated EF_i at each 10 nm reaches its highest values at the wavelengths where the electric field distribution shows a resonant behaviour. For example, $EF_i = 10.48n^2$ at 1130 nm, that is almost three times higher than EF_{Green} . Comparing our results to the TCM theory, up to 1050–1070 nm, the modelled EF_i are mostly within the theoretical curve carried out for b_2 and follow also the discontinuity foreseen by TCM theory. In fact, passing from 990 nm to 1000 nm, the number of leakage channels suddenly decreases, leading to a higher theoretical EF for $\lambda > 1000$ nm. On the other hand, beyond 1050–1070 nm, the EF_i of both modelled spectra is consistently well above both TCM-based EF s, indicating a superposition of effects due to both front and rear gratings. The latter finding should not surprise, since (i) the TCM theory was developed for one-sided textured dielectric slabs with perfect electrical conductor as ideal rear mirror, and (ii) the structure of the nc-Si:H thin-film solar cell might not operate in the over-coupling regime, due to the presence of front supporting layers acting as (weak) cladding against optical leakage. This highlights the need to modify the TCM theory, extending its validity to the case of decoupled front/back texturing and finding out whether the threshold range 1050–1070 nm only conveniently points at the (weighted) average of the front and rear grating or if it has a deeper physical meaning.

3.3. Wave-guided modes

Supported by wave-guide mode theory, we here discuss the nature and the energy position of absorption peaks observed in both 10-nm and 1-nm stepped A_i spectra of the best modelled structure for $\lambda > 950$ nm, allowing for absorption gains beyond the *Green* limit.

According to reflection pole method (RPM) calculations (see Section 2.6), all modes supported by the absorber are plotted in the dispersion diagram depicted in Fig. 8. Red lines represent modes for s-polarized light, while blue lines refer to those for p-polarized light. Vertical lines, representing the centre of Brillouin zones of the front (light green) and back textures (dark green), are also reported. Continuous lines indicate Brillouin zone centres distanced by $2\pi/b_m$, while dashed lines represent zone centre with distance $2\sqrt{2}\pi/b_m$, where b_m is the texture period at the front ($m = 1$) or at the back side ($m = 2$) of the absorber layer (see inset in Fig. 8). In black, light lines are depicted, representing the

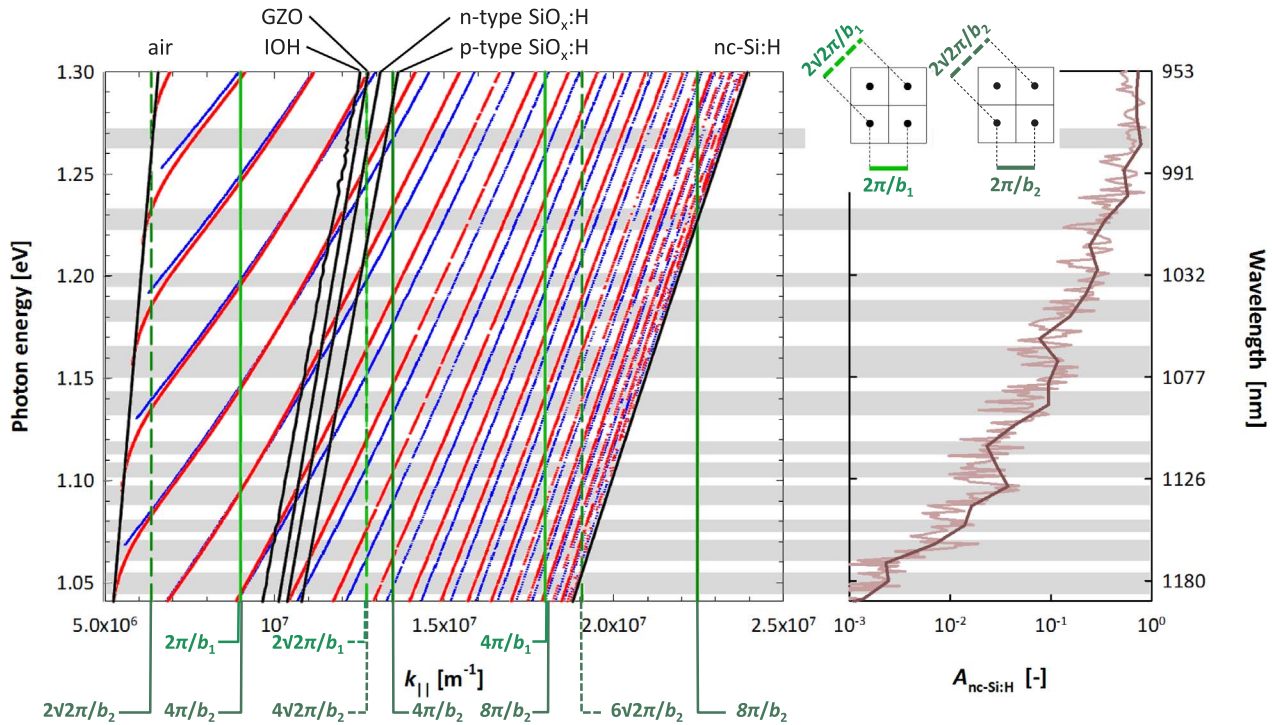


Fig. 8. Dispersion diagram (left panel) and absorption curve (right panel) of the structure with optimized surface morphology (structure #2), supporting materials as in design IV, and 40-nm thick front IOH. Oblique black curves are light lines of each layer of interest, calculated with Eq. (13). Vertical green lines represent the centre of square Brillouin zones of the front and back textures (sketched in the inset), where b_1 and b_2 are the periods of the front and back texture, respectively. The intersection between the centre of a Brillouin zone and an available wave-guided p- (blue) or s-polarization mode (red) represent the excitation of a resonance. Brillouin-zone/mode intersections closer to the light-line of p-type $\text{SiO}_x\text{:H}$, which result in higher resonance intensity (Naqavi et al., 2013, 2014), are correlated to peaks in the absorption graph by grey bands. In the absorption plot, the dark brown curve indicates results of the simulation carried out every 10 nm, while the light brown line refers to a simulation conducted with a resolution of 1 nm.

maximum allowed value of $k_{||}$ at a specific photon energy E , for a given material with refractive index n ($k_{||} = E \cdot 2\pi n / hc$, where $h = 6.63 \times 10^{-34}$ J s is Planck's constant, and $c = 2.998 \times 10^8$ m/s is the speed of light *in vacuo*). Between the light lines of p-doped nc- $\text{SiO}_x\text{:H}$ and nc-Si:H, the intersection between the centre of Brillouin zones and the available dispersion modes in nc-Si:H represents the excitation of a guided mode in the absorber. In turn, this is expected to cause a significant increase of absorption at the corresponding wavelength/photon energy. In the plot, grey bands indicate these intersections, and the corresponding peak(s) in the absorption plot (on the right panel of Fig. 8). Due to several approximations, mainly the resolution of simulations and calculations and the fact that the RPM assumes flat interfaces, instead of individuating the exact photon energy at which a resonance is taking place, it was preferred to provide energy bands where those resonances are likely to happen. Moreover, modes that are excited closer to the light line of p-doped nc- $\text{SiO}_x\text{:H}$ layer, are coupled more strongly to the absorber (Naqavi et al., 2013; Naqavi et al., 2014), hence only those were considered. It is important to note that Brillouin zones from both the front- and the back-surface textures are of influence. This means that a concurrent excitation of waveguide modes takes place in our decoupled front and rear textured device. In other words, both the front and the rear gratings work together mutually reinforcing the excitation.

3.4. Light trapping efficiency (LTE)

Having established the best structure from phase *three* of this study, we proceed with the calculation of the LTE (see Eq. (9), Section 2.5). Note that the optical thickness (t_{opt}) of the absorber for the geometry in structure #2 is 2693.2 nm (see Section 2.3). The implied photocurrent density of the flat equivalent (FE) structure (see Section 2.4) was obtained by 3-D simulation ($J_{\text{FE}} = 23.05 \text{ mA/cm}^2$) while that of the double pass ($J_{\text{DP}} = 24.72 \text{ mA/cm}^2$) was carried out from Eq. (5). J_{DP} is slightly

higher than J_{FE} due to the assumptions on ideal front in-coupling and back reflection as well as the absence of supporting layers. The Green limit evaluated at perpendicular incidence predicts $J_{\text{Green}} = 35.89 \text{ mA/cm}^2$, while the performance of our best design yields $J_{\text{ph-i}} = 36.00 \text{ mA/cm}^2$. Finally, we obtain a $\text{LTE} = 1.16$. It is worth mentioning that the outcome of an LTE greater than unity is not an anomaly. It means that the surface structure exhibits better light trapping properties than an ideal Lambertian scatterer. Further, we emphasize that, to the best of our knowledge, no study has been able to achieve thus far an $\text{LTE} > 1$, especially for an optical system modelling a fully-functional solar cell.

3.5. Angle of incidence

Solar cells are optimized to perform best under perpendicularly incident sunlight. However, for textured cells this may no longer be the case. In fact, incident light may be trapped inside the cell more efficiently when light impinges on a device with an angle of incidence (AOI) $> 0^\circ$. This is mainly because lower order diffraction modes (i.e. more energetic) may be trapped instead of being reflected at high AOI. In Fig. 9, the performance of our textured solar cell is reported as function of AOI and in terms of deviation from the Green limit. The best optical result was achieved for AOI = -30° , yielding $\Delta\text{Green} = 2.64\%$ and $J_{\text{ph-i}} = 36.84 \text{ mA/cm}^2$. This result indicates that it may be possible to find an optimal morphology for operation at AOI $> 0^\circ$, with an absorption enhancement far greater than that obtained here. Also, it is evident that the modelled solar cell performs differently for positive and negative angles. due to the misalignment (asymmetry) between top and bottom textures. Finally, it can be noted that absorption is enhanced beyond the perpendicular incidence performance for a very wide range of AOI, up $\pm 60^\circ$, consistent with the findings of (Yu et al., 2010a). This result is especially promising for PV systems that do not employ auxiliary tracking mounting and yet exhibit tracking-like high

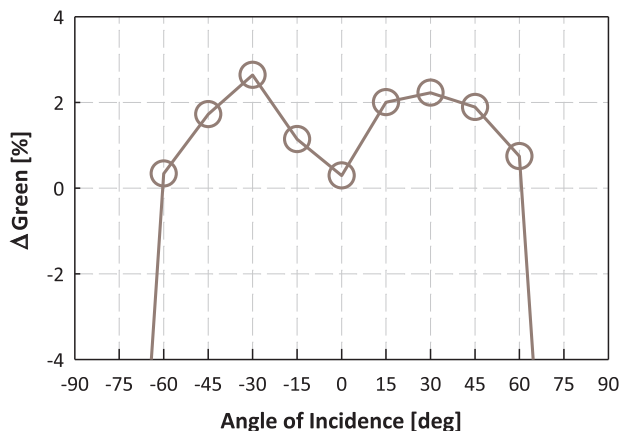


Fig. 9. Deviation ($\Delta Green$) of the implied i-layer photocurrent density ($J_{ph,i}$) from the *Green* limit (calculated assuming perpendicular incidence), as function of the angle of incidence of light.

performance.

4. Conclusions and outlook

We have successfully created an optical model representing a fully functional thin-film nc-Si:H solar cell with a 2- μm thick absorber layer. Using this model, we optimized surface morphologies with high aspect ratio pyramids at the front – to ensure optimal in-coupling of light into the absorber – and shallow, large pyramids on the back surface of the cell, for the scattering and trapping of near infrared photons inside the active layer. Furthermore, we optimized the materials constituting the doped layers and the back TCO, as well as the thickness of the front TCO. By convoluting the simulated absorbance spectra between 300 and 1200 nm with the AM1.5 reference photon flux, we achieved an implied photocurrent density that is 0.31% higher than that calculated for the *Green* limit, using the same optical thickness and within the same wavelength range. Finally, our results predict high absorption over a wide range of angles of incident light, as well as an additional enhancement under non-perpendicular angles. For an angle of incidence equal to -30° , it should be possible to generate a photocurrent density as large as 36.84 mA/cm^2 , which is 2.64% higher than that given by the *Green* limit at perpendicular incidence. This means a massive improvement compared to current photocurrent densities in thin-film nc-Si:H solar cells which generally lie around 29 mA/cm^2 for the considered thickness (Sai et al., 2015). For the best simulated 10-nm stepped A_1 spectrum perpendicularly illuminated, the strongest light trapping enhancement factor with a magnitude of 131.3 is predicted to appear at a wavelength of 1130 nm. According to our knowledge, this is the strongest simulated absorption enhancement achieved for a model of a fully-functional nc-Si:H solar cell. For explaining the high enhancement factor observed in our decoupled front and rear textured dielectric slab, the temporal mode-coupled theory must be modified to accommodate the concurrent influence of front and rear texture. This is evident by analysing wave-guide modes, that are excited in same energy ranges by both front and rear textures.

We emphasize that these results were obtained using only the properties of real materials that are also already proven to work in state-of-the-art thin-film silicon solar cells. On the other hand, it is known that electrical performance may collapse owing to defective areas in the absorber material because of growth on high aspect ratio features (Python et al., 2008) or thicker absorber thickness than lateral dimensions of the features. Therefore, our proposed solar cells design can either be regarded as upper limit for thin-film silicon absorber materials or can be re-imagined for ultra-thin epitaxially grown silicon absorber, where the crystal structure is maintained and the build quality of the surface features can be kept high with similar etching

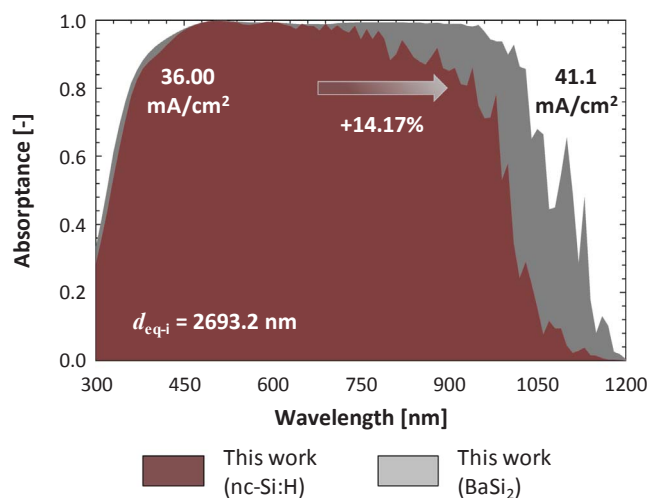


Fig. 10. Given the same 3-D model (structure #2, design #4, 40-nm thick front IOH) with the same supporting layers, absorbance comparison between nc-Si:H and BaSi_2 absorbers, both 2- μm thick ($t_{opt} = 2693.2 \text{ nm}$). A 14.17% improvement in the implied photocurrent density is predicted switching from nc-Si:H (36 mA/cm^2) to BaSi_2 (41.1 mA/cm^2). The region of high absorption in case of BaSi_2 extends from 650 nm to 950 nm, mainly owing to the much higher absorption coefficient of BaSi_2 with respect to that of nc-Si:H (46 times higher at 770 nm).

processes as in case of bulk material. Another option can be to look at new semiconducting materials with better light absorption properties than nc-Si:H. In fact, preliminary modelling work on BaSi_2 -based devices, where the same light trapping scheme proposed in this work was applied, showed that implied photocurrent densities up to 41.1 mA/cm^2 can be achieved, for absorber thicknesses of 2 μm (Vismara et al., 2016) (see Fig. 10). Solar cells based on our advanced light trapping scheme, endowed with nc-Si:H, epi-grown Si or BaSi_2 , can be used as a bottom sub-cell in thin-film multi-junction devices enabling highly efficient solar-to-electricity conversion.

Acknowledgements

The authors thank dr. Franz-Josef Haug (EPFL, Switzerland), dr. Ali Naqavi (Caltech, U.S.A.), dr. Hitoshi Sai (AIST, Japan), dr. Klaus Jäger (HZB, Germany), dr. Corsin Battaglia (EMPA, Switzerland), prof. dr. Eli Yablonovitch (UC Berkeley, U.S.A.) and prof. dr. Harry Atwater (Caltech, U.S.A.) for useful and stimulating discussions. S. F. acknowledges the support of U. S. Department of Energy Grant No. DE-FG-07ER46426.

References

- Alta Devices, 2013. Press release 2013-03-04. <http://www.altadevices.com/altadevices-achieves-30-8-efficiency-record-with-new-generation-solar-cell-technology/> (Accessed 25 October 2017).
- Anemogiannis, E., Glytsis, E.N., Gaylord, T.K., 1999. Determination of guided and leaky modes in lossless and lossy planar multilayer optical waveguides: reflection pole method and wavevector density method. *J. Lightwave Technol.* 17 (5), 929.
- ANSYS, ANSYS HFSS White papers. < <http://www.ansys.com/Products/Electronics/ANSYS-HFSS> > (Accessed 25 October 2017).
- Battaglia, C., Cuevas, A., De Wolf, S., 2016. High-efficiency crystalline silicon solar cells: status and perspectives. *Energy Environ. Sci.* 9 (5), 1552–1576.
- Battaglia, C., Escarré, J., Söderström, K., Erni, L., Ding, L., Bugnon, G., Billet, A., Boccard, M., Barraud, L., De Wolf, S., 2011. Nanoimprint lithography for high-efficiency thin-film silicon solar cells. *Nano Lett.* 11 (EPFL-ARTICLE-163046) 661.
- Battaglia, C., Hsu, C.-M., Söderström, K., Escarré, J., Haug, F.-J., Charrière, M., Boccard, M., Despeisse, M., Alexander, D.T.L., Cantoni, M., Cui, Y., Ballif, C., 2012. Light trapping in solar cells: can periodic beat random? *ACS Nano* 6 (3), 2790–2797.
- Berginski, M., Hüpkens, J., Reetz, W., Rech, B., Wuttig, M., 2008. Recent development on surface-textured ZnO: Al films prepared by sputtering for thin-film solar cell application. *Thin Solid Films* 516 (17), 5836–5841.
- Biswas, R., Xu, C., 2011. Nano-crystalline silicon solar cell architecture with absorption at the classical 4n 2 limit. *Opt. Express* 19 (104), A664–A672.
- Boccard, M., Battaglia, C., Hänni, S., Söderström, K., Escarré, J., Nicolay, S., Meillaud, F.,

- Despeisse, M., Ballif, C., 2012. Multiscale transparent electrode architecture for efficient light management and carrier collection in solar cells. *Nano Lett.* 12(EPL-ARTICLE-177046) 1344–1348.
- Brongersma, M.L., Cui, Y., Fan, S., 2014. Light management for photovoltaics using high-index nanostructures. *Nat. Mater.* 13 (5), 451–460.
- Davidson, D.B., 2010. *Computational Electromagnetics for RF and Microwave Engineering*. Cambridge University Press.
- Demontis, V., Sanna, C., Melskens, J., Santbergen, R., Smets, A.H.M., Damiano, A., Zeman, M., 2013. The role of oxide interlayers in back reflector configurations for amorphous silicon solar cells. *J. Appl. Phys.* 113 (6), 064508.
- Ferry, V.E., Verschuren, M.A., Li, H.B.T., Schropp, R.E.I., Atwater, H.A., Polman, A., 2009. Improved red-response in thin film a-Si: H solar cells with soft-imprinted plasmonic back reflectors. *Appl. Phys. Lett.* 95 (18), 183503.
- Solar, First., 2016. Press release 2016-02-23. <https://www.greentechmedia.com/articles/read/first-solar-hits-record-22-1-conversion-efficiency-for-cdte-solar-cell> Accessed 25 October 2017.
- Fraunhofer, I.S.E., 2017. Photovoltaic Report. <http://www.ise.fraunhofer.de/en/downloads-englisch/pdf-files-englisch/photovoltaics-report-slides.pdf> Accessed 25 October 2017.
- Fujiwara, H., Kondo, M., 2005. Effects of carrier concentration on the dielectric function of ZnO: Ga and In₂O₃:Sn studied by spectroscopic ellipsometry: Analysis of free-carrier and band-edge absorption. *Physical Review B* 71 (7), 075109.
- Gabriel, O., Kirner, S., Leendertz, C., Gerhardt, M., Heidelberg, A., Bloes, H., Schlattmann, R., Rech, B., 2011. Large area PECVD of a-Si H/a-Si H tandem solar cells. *physica status solidi (c)*. 8 (10), 2982–2985.
- Glunz, S., Feldmann, F., Richter, A., Bivour, M., Reichel, C., Steinkemper, H., Benick, J., Hermle, M., 2015. The irresistible charm of a simple current flow pattern—25% with a solar cell featuring a full-area back contact, Proceedings of the 31st European Photovoltaic Solar Energy Conference and Exhibition. pp. 259–263.
- Green, M.A., 2002. Lambertian light trapping in textured solar cells and light-emitting diodes: analytical solutions. *Prog. Photovoltaics Res. Appl.* 10 (4), 235–241.
- Guha, S., Yang, J., 2005. High-Efficiency Amorphous Silicon Alloy Based Solar Cells and Modules Final Technical Progress Report 30 May 2002–31 May 2005.
- Haug, F.-J., Ballif, C., 2015. Light management in thin film silicon solar cells. *Energy Environ. Sci.* 8 (3), 824–837.
- Haug, F.-J., Naqvi, A., Ballif, C., 2012. Diffraction and absorption enhancement from textured back reflectors of thin film solar cells. *J. Appl. Phys.* 112 (2), 024516.
- Haug, F.-J., Söderström, K., Naqvi, A., Ballif, C., 2011a. Resonances and absorption enhancement in thin film silicon solar cells with periodic interface texture. *J. Appl. Phys.* 109 (8), 084516.
- Haug, F.-J., Söderström, T., Cubero, O., Terrazoni-Daudrix, V., Ballif, C., 2009. Influence of the ZnO buffer on the guided mode structure in Si/ZnO/Ag multilayers. *J. Appl. Phys.* 106 (4), 044502.
- Haug, F.J., Söderström, K., Naqvi, A., Ballif, C., 2011. Excitation of guided-mode resonances in thin film silicon solar cells. *MRS Proceedings* 1321.
- Holman, Z.C., Descoedres, A., De Wolf, S., Ballif, C., 2013. Record infrared internal quantum efficiency in silicon heterojunction solar cells with dielectric/metal rear reflectors. *IEEE J. Photovoltaics* 3 (4), 1243–1249.
- Hongsingthong, A., Krajangsang, T., Yunaz, I.A., Miyajima, S., Konagai, M., 2010. ZnO films with very high haze value for use as front transparent conductive oxide films in thin-film silicon solar cells. *Appl. Phys. Express* 3 (5), 051102.
- Ingenito, A., Isabella, O., Zeman, M., 2014. Experimental demonstration of $4n^2$ classical absorption limit in nanotextured ultrathin solar cells with dielectric omnidirectional back reflector. *ACS Photon.* 1 (3), 270–278.
- Ingenito, A., Isabella, O., Zeman, M., 2015. Nano-cones on micro-pyramids: modulated surface textures for maximal spectral response and high-efficiency solar cells. *Prog. Photovoltaics Res. Appl.* 23 (11), 1649–1659.
- Isabella, O., 2013. *Light Management in Thin-Film Silicon Solar Cells*, Photovoltaic Materials and Devices. Delft University of Technology, Delft.
- Isabella, O., Campa, A., Heijna, M., Soppe, W., van Erven, R., Franken, R., Borg, H., Zeman, M., 2008. Diffraction gratings for light trapping in thin-film silicon solar cells. In: *Conference Record of the 23rd European Photovoltaic Solar Energy Conference*. pp. 2320–2324.
- Isabella, O., Liu, P., Bolman, B., Krc, J., Smets, A., Zeman, M., 2011. Modulated surface-textured substrates with high haze: from concept to application in thin-film silicon solar cells. In: *2011 37th IEEE Photovoltaic Specialists Conference (PVSC)*. IEEE, pp. 000616-000621.
- Isabella, O., Moll, F., Krč, J., Zeman, M., 2010. Modulated surface textures using zinc-oxide films for solar cells applications. *Physica Status Solidi (a)* 207 (3), 642–646.
- Isabella, O., Sai, H., Kondo, M., Zeman, M., 2014a. Full-wave optoelectrical modeling of optimized flattened light-scattering substrate for high efficiency thin-film silicon solar cells. *Prog. Photovoltaics Res. Appl.* 22 (6), 671–689.
- Isabella, O., Smets, A.H.M., Zeman, M., 2014b. Thin-film silicon-based quadruple junction solar cells approaching 20% conversion efficiency. *Sol. Energy Mater. Sol. Cells* 129, 82–89.
- Isabella, O., Solntsev, S., Caratelli, D., Zeman, M., 2012. 3-D optical modeling of single and multi-junction thin-film silicon solar cells on gratings. *MRS Online Proc. Library Arch.* 1426, 149–154.
- Isabella, O., Solntsev, S., Caratelli, D., Zeman, M., 2013. 3-D optical modeling of thin-film silicon solar cells on diffraction gratings. *Prog. Photovoltaics Res. Appl.* 21 (1), 94–108.
- Isabella, O., Vismara, R., Ingenito, A., Rezaei, N., Zeman, M., 2016. Decoupled front/back dielectric textures for flat ultra-thin c-Si solar cells. *Opt. Express* 24 (6), A708–A719.
- ITRPV Eighth Edition, 2017. *International Technology Roadmap for Photovoltaics Results 2016 incl. Maturity Report*. < <http://www.itrpv.net/Reports/Downloads/> > . (Accessed 25 October 2017).
- Jäger, K., Isabella, O., Swaaij, R.A.C.M.M.v., Zeman, M., 2011. Angular resolved scattering measurements of nano-textured substrates in a broad wavelength range. *Meas. Sci. Technol.* 22 (10), 105601.
- Jäger, K., Lenns, J., Veltman, P., Hamers, E., 2013. Large-area production of highly efficient flexible light-weight thin-film silicon PV modules, Proc. 28th European Photovoltaic Solar Energy Conf., Paris, France. pp. 2164–2169.
- Kakinuma, H., Nishikawa, S., Watanabe, T., 1983. Thickness dependence of Staebler-Wronski effect in a-Si: H. *J. Non-Cryst. Solids* 59, 421–424.
- Kambe, M., Takahashi, A., Taneda, N., Masumo, K., Oyama, T., Sato, K., 2008. Fabrication of a-Si: H solar cells on high haze SnO₂: F thin films. In: *33rd IEEE Photovoltaic Specialists Conference, 2008. PVSC'08*. IEEE, pp. 1–4.
- Kim, S., Chung, J.-W., Lee, H., Park, J., Heo, Y., Lee, H.-M., 2013. Remarkable progress in thin-film silicon solar cells using high-efficiency triple-junction technology. *Sol. Energy Mater. Sol. Cells* 119, 26–35.
- Kirner, S., Neubert, S., Schultz, C., Gabriel, O., Stannowski, B., Rech, B., Schlattmann, R., 2015. Quadruple-junction solar cells and modules based on amorphous and microcrystalline silicon with high stable efficiencies. *Jpn. J. Appl. Phys.* 54 (8S1), 08KB03.
- Koida, T., Fujiwara, H., Kondo, M., 2008. Reduction of optical loss in hydrogenated amorphous silicon/crystalline silicon heterojunction solar cells by high-mobility hydrogen-doped In₂O₃ transparent conductive oxide. *Appl. Phys. Express* 1 (4), 041501.
- Lipovšek, B., Cvek, M., Čampa, A., Krč, J., Topič, M., 2010. Analysis and Optimisation of Periodic Interface Textures in Thin-Film Silicon Solar Cells. In: *25th European Photovoltaic Solar Energy Conference, Valencia, Spain*.
- Liu, B., Bai, L., Chen, Z., Zhang, X., Zhang, D., Ni, J., Huang, Q., Wei, C., Sun, J., Chen, X., Ren, H., Hou, G., Wang, G., Zhao, Y., 2015. High efficiency triple junction thin film silicon solar cells with optimized electrical structure. *Prog. Photovoltaics Res. Appl.* 23 (10), 1313–1322.
- Liu, B., Bai, L., Li, T., Wei, C., Li, B., Huang, Q., Zhang, D., Wang, G., Zhao, Y., Zhang, X., 2017. High efficiency and high open-circuit voltage quadruple-junction silicon thin film solar cells for future electronic applications. *Energy Environ. Sci.* 10 (5), 1134–1141.
- Martins, E.R., Li, J., Liu, Y., Depauw, V., Chen, Z., Zhou, J., Krauss, T.F., 2012. Deterministic quasi-random nanostructures for photon control. *Nat. Commun.* 4, 2665-2665.
- Masuko, K., Shigematsu, M., Hashiguchi, T., Fujishima, D., Kai, M., Yoshimura, N., Yamaguchi, T., Ichihashi, Y., Mishima, T., Matsubara, N., 2014. Achievement of more than 25% conversion efficiency with crystalline silicon heterojunction solar cell. *IEEE J. Photovoltaics* 4 (6), 1433–1435.
- Matsui, T., Maejima, K., Bidville, A., Sai, H., Koida, T., Suezaki, T., Matsumoto, M., Saito, K., Yoshida, I., Kondo, M., 2015. High-efficiency thin-film silicon solar cells realized by integrating stable a-Si H absorbers into improved device design. *Jpn. J. Appl. Phys.* 54 (8S1), 08KB10.
- Matsui, T., Sai, H., Saito, K., Kondo, M., 2013. High-efficiency thin-film silicon solar cells with improved light-soaking stability. *Prog. Photovoltaics Res. Appl.* 21 (6), 1363–1369.
- Mellor, A., Tobias, I., Martí, A., Mendes, M.J., Luque, A., 2011. Upper limits to absorption enhancement in thick solar cells using diffraction gratings. *Prog. Photovoltaics Res. Appl.* 19 (6), 676–687.
- Melskens, J., Schouten, M., Mannheim, A., Vullers, A.S., Mohammadian, Y., Eijt, S.W., Schut, H., Matsui, T., Zeman, M., Smets, A.H., 2014. The nature and the kinetics of light-induced defect creation in hydrogenated amorphous silicon films and solar cells. *IEEE J. Photovoltaics* 4 (6), 1331–1336.
- Naqvi, A., Haug, F.-J., Ballif, C., Scharf, T., Herzog, H.P., 2013. Limit of light coupling strength in solar cells. *Appl. Phys. Lett.* 102 (13), 131113.
- Naqvi, A., Haug, F.-J., Söderström, K., Battaglia, C., Paeder, V., Scharf, T., Herzog, H.P., Ballif, C., 2014. Angular behavior of the absorption limit in thin film silicon solar cells. *Prog. Photovoltaics Res. Appl.* 22 (11), 1147–1158.
- NREL, Reference Solar Spectral Irradiance: Air Mass 1.5, < <http://redc.nrel.gov/solar/spectra/am1.5/> > . (Accessed 25 October 2017).
- Paetzold, U.W., Moulin, E., Michaelis, D., Böttler, W., Wächter, C., Hagemann, V., Meier, M., Carius, R., Rau, U., 2011. Plasmonic reflection grating back contacts for microcrystalline silicon solar cells. *Appl. Phys. Lett.* 99 (18), 181105.
- Pahud, C., Isabella, O., Naqvi, A., Haug, F.-J., Zeman, M., Herzog, H.P., Ballif, C., 2013. Plasmonic silicon solar cells: impact of material quality and geometry. *Opt. Express* 21 (105), A786–A797.
- Python, M., Vallat-Sauvain, E., Bailat, J., Dominé, D., Fesquet, L., Shah, A., Ballif, C., 2008. Relation between substrate surface morphology and microcrystalline silicon solar cell performance. *J. Non-Cryst. Solids* 354 (19), 2258–2262.
- Ritz, W., 1909. Über eine neue Methode zur Lösung gewisser Variationsprobleme der mathematischen Physik. *Journal für die reine und angewandte Mathematik* 135, 1–61.
- Sai, H., Koida, T., Matsui, T., Yoshida, I., Saito, K., Kondo, M., 2013a. Microcrystalline silicon solar cells with 10.5% efficiency realized by improved photon absorption via periodic textures and highly transparent conductive oxide. *Appl. Phys. Express* 6 (10), 104101.
- Sai, H., Maejima, K., Matsui, T., Koida, T., Kondo, M., Nakao, S., Takeuchi, Y., Katayama, H., Yoshida, I., 2015. High-efficiency microcrystalline silicon solar cells on honeycomb textured substrates grown with high-rate VHF plasma-enhanced chemical vapor deposition. *Jpn. J. Appl. Phys.* 54 (8S1), 08KB05.
- Sai, H., Matsui, T., Matsubara, K., 2016. Stabilized 14.0%-efficient triple-junction thin-film silicon solar cell. *Appl. Phys. Lett.* 109 (18), 183506.
- Sai, H., Saito, K., Hozuki, N., Kondo, M., 2013b. Relationship between the cell thickness and the optimum period of textured back reflectors in thin-film microcrystalline silicon solar cells. *Appl. Phys. Lett.* 102 (5), 053509.
- Santbergen, R., Tan, H., Zeman, M., Smets, A.H., 2014. Enhancing the driving field for

- plasmonic nanoparticles in thin-film solar cells. *Opt. Express* 22 (104), A1023–A1028.
- Sato, K., Gotoh, Y., Wakayama, Y., Hayashi, Y., Adachi, K., Nishimura, H., 1992. Highly textured SnO₂: F TCO films for a-Si solar cells. *Rep. Res. Lab. Asahi Glass Co. Ltd* 42, 129–137.
- Schuster, C.S., Bozzola, A., Andreani, L.C., Krauss, T.F., 2014. How to assess light trapping structures versus a Lambertian Scatterer for solar cells? *Opt. Express* 22 (102), A542–A551.
- Schüttauf, J.-W., Niesen, B., Löfgren, L., Bonnet-Eymard, M., Stuckelberger, M., Hänni, S., Boccard, M., Bugnon, G., Despeisse, M., Haug, F.-J., 2015. Amorphous silicon-germanium for triple and quadruple junction thin-film silicon based solar cells. *Sol. Energy Mater. Sol. Cells* 133, 163–169.
- Shakir, S.A., Turner, A.F., 1982. Method of poles for multilayer thin-film waveguides. *Appl. Phys. A* 29 (3), 151–155.
- Si, F.T., Isabella, O., Tan, H., Zeman, M., 2017. Quadruple-Junction Thin-Film Silicon Solar Cells Using Four Different Absorber Materials. *Solar RRL* 1(3–4), 1700036-n/a.
- Si, F.T., Kim, D.Y., Santbergen, R., Tan, H., van Swaaij, R.A., Smets, A.H., Isabella, O., Zeman, M., 2014. Quadruple-junction thin-film silicon-based solar cells with high open-circuit voltage. *Appl. Phys. Lett.* 105 (6), 063902.
- Söderström, K., 2013. Coupling light into thin silicon layers for high-efficiency solar cells. *École Polytechnique Fédérale de Lausanne*.
- Söderström, K., Bugnon, G., Biron, R., Pahud, C., Meillaud, F., Haug, F.-J., Ballif, C., 2012. Thin-film silicon triple-junction solar cell with 12.5% stable efficiency on innovative flat light-scattering substrate. *J. Appl. Phys.* 112 (11), 114503.
- Söderström, K., Haug, F.-J., Escarré, J., Cubero, O., Ballif, C., 2010. Photocurrent increase in n-i-p thin film silicon solar cells by guided mode excitation via grating coupler. *Appl. Phys. Lett.* 96 (21), 213508.
- Söderström, T., Haug, F.J., Niquille, X., Ballif, C., 2009. TCOs for nip thin film silicon solar cells. *Prog. Photovoltaics Res. Appl.* 17 (3), 165–176.
- Frontier, Solar., 2015. Press release 2015-12-08. <http://www.solar-frontier.com/eng/news/2015/C051171.html> Accessed 25 October 2017.
- Springer, J., Poruba, A., Müllerova, L., Vanecek, M., Kluth, O., Rech, B., 2004. Absorption loss at nanorough silver back reflector of thin-film silicon solar cells. *J. Appl. Phys.* 95 (3), 1427–1429.
- Staebler, D., Wronski, C.R., 1980. Optically induced conductivity changes in discharge-produced hydrogenated amorphous silicon. *J. Appl. Phys.* 51 (6), 3262–3268.
- Stuckelberger, M., Despeisse, M., Bugnon, G., Schüttauf, J.-W., Haug, F.-J., Ballif, C., 2013. Comparison of amorphous silicon absorber materials: light-induced degradation and solar cell efficiency. *J. Appl. Phys.* 114 (15), 154509.
- Suemasu, T., 2015. Exploring the possibility of semiconducting BaSi₂ for thin-film solar cell applications. *Jpn. J. Appl. Phys.* 54 (7S2), 07JA01.
- Suh, W., Wang, Z., Fan, S., 2004. Temporal coupled-mode theory and the presence of non-orthogonal modes in lossless multimode cavities. *IEEE J. Quantum Electron.* 40 (10), 1511–1518.
- Tan, H., Moulin, E., Si, F.T., Schüttauf, J.-W., Stuckelberger, M., Isabella, O., Haug, F.-J., Ballif, C., Zeman, M., Smets, A.H.M., 2015. Highly transparent modulated surface textured front electrodes for high-efficiency multijunction thin-film silicon solar cells. *Prog. Photovoltaics Res. Appl.* 23 (8), 949–963.
- Tan, H., Psomadaki, E., Isabella, O., Fischer, M., Babal, P., Vasudevan, R., Zeman, M., Smets, A.H.M., 2013. Micro-textures for efficient light trapping and improved electrical performance in thin-film nanocrystalline silicon solar cells. *Appl. Phys. Lett.* 103 (17), 173905.
- Tan, H., Santbergen, R., Smets, A.H., Zeman, M., 2012. Plasmonic light trapping in thin-film silicon solar cells with improved self-assembled silver nanoparticles. *Nano Lett.* 12 (8), 4070–4076.
- TEL Solar, 2014. Press release 2014-06-14. http://research.omicsgroup.org/index.php/TEL_Solar Accessed 25 October 2017.
- Tiedje, T., Yablonoitch, E., Cody, G.D., Brooks, B.G., 1984. Limiting efficiency of silicon solar cells. *IEEE Trans. Electron Devices* 31 (5), 711–716.
- van Erven, A., Rutten, J., van der Hofstad, G., de Groot, H., Steltenpool, M., De Ruijter, J., Titulaer, B., Borg, H., Rajeswaran, G., 2010. Light-trapping enhancement by diffractive textures for thin-film silicon solar cells. In: *Proceedings of the 25th European Photovoltaic Solar Energy Conference*. pp. 3181–3184.
- Vetter, M., Borrajo, J., Mata, C., Andreu, J., 2009. Progress in the fabrication of amorphous silicon photovoltaic modules on very large 2, 60m x 2, 20m glass substrates. In: *Proc. 24th Europ. Photovoltaic Solar Energy Conference and Exhibition, Hamburg*. p. 25.
- Vismara, R., Isabella, O., Zeman, M., 2016. Organometallic Halide Perovskite/Barium Disilicide Thin-Film Double-Junction Solar Cells. *SPIE, SPIE Photonics Europe*, pp. 9.
- Wang, K.X., Yu, Z., Liu, V., Cui, Y., Fan, S., 2012. Absorption enhancement in ultrathin crystalline silicon solar cells with antireflection and light-trapping nanocone gratings. *Nano Lett.* 12 (3), 1616–1619.
- Weiland, T., 1977. A discretization model for the solution of Maxwell's equations for six-component fields. *Archiv Elektronik und Uebertragungstechnik* 31, 116–120.
- Yamamoto, K., 2015. 25.1% efficiency Cu metallized heterojunction crystalline silicon solar cell. In: *25th International Photovoltaic Science and Engineering Conference, Busan, Korea*.
- Yamamoto, K., Nakajima, A., Yoshimi, M., Sawada, T., Fukuda, S., Suezaki, T., Ichikawa, M., Koi, Y., Goto, M., Meguro, T., Matsuda, T., Kondo, M., Sasaki, T., Tawada, Y., 2005. A thin-film silicon solar cell and module. *Prog. Photovoltaics Res. Appl.* 13 (6), 489–494.
- Yan, B., Yue, G., Sivec, L., Yang, J., Guha, S., Jiang, C.-S., 2011. Innovative dual function nc-SiOx: H layer leading to a > 16% efficient multi-junction thin-film silicon solar cell. *Appl. Phys. Lett.* 99 (11), 113512.
- Yang, W.S., Noh, J.H., Jeon, N.J., Kim, Y.C., Ryu, S., Seo, J., Seok, S.I., 2015. High-performance photovoltaic perovskite layers fabricated through intramolecular exchange. *Science* 348 (6240), 1234–1237.
- Yee, K., 1966. Numerical solution of initial boundary value problems involving Maxwell's equations in isotropic media. *IEEE Transaction Antennas Propagation AP-14*: 302–307 3. On implementing a numeric Huygen's source scheme in a finite difference program to illuminate scattering bodies'. *IEEE Trans. Nucl. Sci.* 27, 1829–1833.
- Yoshikawa, K., Kawasaki, H., Yoshida, W., Irie, T., Konishi, K., Nakano, K., Uto, T., Adachi, D., Kanematsu, M., Uzu, H., 2017. Silicon heterojunction solar cell with interdigitated back contacts for a photoconversion efficiency over 26%. *Nat. Energy* 2, 17032.
- Yu, Z., Fan, S., 2011. Angular constraint on light-trapping absorption enhancement in solar cells. *Appl. Phys. Lett.* 98 (1), 011106.
- Yu, Z., Raman, A., Fan, S., 2010a. Fundamental limit of light trapping in grating structures. *Opt. Express* 18 (S3), A366–A380.
- Yu, Z., Raman, A., Fan, S., 2010b. Fundamental limit of nanophotonic light trapping in solar cells. *Proc. Natl. Acad. Sci.* 107 (41), 17491–17496.
- Zeman, M., Isabella, O., Solntsev, S., Jäger, K., 2013. Modelling of thin-film silicon solar cells. *Sol. Energy Mater. Sol. Cells* 119 (Supplement C), 94–111.
- Zhao, J., Wang, A., Green, M.A., Ferrazza, F., 1998. 19.8% efficient “honeycomb” textured multicrystalline and 24.4% monocrystalline silicon solar cells. *Appl. Phys. Lett.* 73 (14), 1991–1993.